# Efficient and stable semitransparent organic photovoltaics with integrated photosynthesis

Yepin Zhao<sup>1, 2†</sup>, Zongqi Li<sup>1, 2†</sup>, Caner Deger<sup>3, 4†</sup>, Minhuan Wang<sup>5\*</sup>, Miroslav Peric<sup>6</sup>, Yanfeng Yin<sup>5</sup>, Dong Meng<sup>1, 2</sup>, Wenxin Yang<sup>1, 2</sup>, Xinyao Wang<sup>1, 2</sup>, Qiyu Xing<sup>1, 2</sup>, Bin Chang<sup>1, 2, 7</sup>, Elizabeth G. Scott<sup>1, 2, 8</sup>, Yifan Zhou<sup>1, 2</sup>, Elizabeth Zhang<sup>1, 2</sup>, Ran Zheng<sup>1, 2</sup>, Jiming Bian<sup>5</sup>, Yantao Shi<sup>9</sup>, Ilhan Yavuz<sup>3\*</sup>, Kung-Hwa Wei<sup>7</sup>, K. N. Houk<sup>4</sup> and Yang Yang<sup>1, 2\*</sup>

Dr. Y. Zhao, Z. Li, W. Yang, X. Wang, Q. Xing, E. G. Scott, Dr. B. Chang, Y. Zhou, Dr. D. Meng, E. Zhang, R. Zheng, and Prof. Y. Yang

<sup>1</sup>Department of Materials Science and Engineering and <sup>2</sup>California NanoSystems Institute, University of California, Los Angeles, Los Angeles, California 90095, United States

#### Dr. C. Deger, Prof. I. Yavuz

<sup>3</sup>Department of Physics, Marmara University, Ziverbey, Istanbul 34722, Turkey

#### Dr. C. Deger, Prof. K. N. Houk

<sup>4</sup>Department of Chemistry and Biochemistry, University of California, Los Angeles, California 90095, United States.

#### Prof. M. Wang, Dr. Y. Yin, Prof. J. Bian

<sup>5</sup>Key Laboratory of Materials Modification by Laser, Ion, and Electron Beams (Dalian University of Technology), Ministry of Education, School of Physics, Dalian, Liaoning Province 116024, China

#### Prof. M. Peric

<sup>6</sup>Department of Physics and Astronomy and The Center for Biological Physics, California State University at Northridge, Northridge, California 91330, United States

#### Dr. B. Chang, Prof. K-H. Wei

<sup>7</sup>Department of Materials Science and Engineering, National Yang Ming Chiao Tung University, Hsinchu 30010, Taiwan

#### E. G. Scott

<sup>8</sup>Department of Electrical Engineering, Columbia University, Northridge, New York, New York 10027, United States

#### Prof. Y. Shi

<sup>9</sup>Key Laboratory of Fine Chemicals, Department of Chemistry, School of Chemical Engineering, Dalian University of Technology, Dalian, Liaoning Province 116024, China

\*Correspondence and requests for materials should be addressed to M.W. (email: wmhkjt@dlut.edu.cn), I.Y. (email: ilhan.yavuz@marmara.edu.tr) or to Y.Y. (email: yangy@ucla.edu)

†These authors contributed equally to this work.

#### Abstract

Semitransparent organic photovoltaics (OPVs) are an emerging solar energy harvesting technology with promising applications such as rooftop energy supplies for the environmentally friendly greenhouses. However, the unfavorable operational stability poses challenges to their feasibility as all-time serving facilities. Here, we report a reductive interlayer structure for the semitransparent solar cells that significantly improves the operational stability under continuous solar radiation. The interlayer effectively suppresses the radical generation from the electron transport layer and prevents the structural decomposition of the organic active layer. The defects that serve as the charge carrier recombination sites are nullified by the electron-donating functional groups of the reduced molecules, which promotes the photovoltaic performances. The semitransparent OPVs demonstrate a power conversion efficiency (PCE) of 13.5% and an average visible transmittance (AVT) of 21.5%, with remarkable operational stability (84.8% retains after 1008 hours) under continuous illumination. Our study shows that the semitransparent OPV roof benefits the survival rate of the crops. Preferable plant growth is realized by the greenhouses with semitransparent OPV roofs compared to that in the traditional glass-roof ones.

#### Main

Food and energy crises have swept most of the developing regions over the world in the recent decades, touching the nerve of every humankind. Sustainable techniques that efficiently utilize farmland are the key to resolving this problem. Greenhouses, in particular, can effectively prolong the cultivation season by remitting the fluctuant weather and/or temperature influence over the crops and vegetables. Thus, it has been widely regarded as an effective strategy to boost the food yield for the growing human population. However, the power grid construction and electricity consumption for the inner environment control of the greenhouses drastically raise the cost, especially in the vast remote regions. Hence, a smart greenhouse with semitransparent photovoltaics as the power-generating roof is exceptionally desirable for modern agriculture.<sup>2,3</sup>

Due to the unique band structure of organic materials, organic photovoltaic (OPV) is able to selectively absorb light with desired wavelength.<sup>4-6</sup> Both the power conversion efficiency (PCEs) and the average visible transmittance (AVT) of the semitransparent OPV have improved substantially in recent years.<sup>7-12</sup> The light weight, low cost, and flexibility of

the semitransparent OPV further guarantee the promising future of its agricultural application. PV-integrated power-generating roof. Is application. Is the widespread use of the semitransparent OPV-integrated power-generating roof. Is One of the major origins of its instability is the photo-degradation of the organic molecules due to the superoxide radicals generated from the ZnO electron transport layer and their corelated diffusion into the organic active layer. In ZnO layer can catalyze the production of superoxide molecules under the sunlight, which attack the reductive organic active layer and break the chemical structure of the organic molecules. In addition to this, the electron-trapping defects in the ZnO layer usually serve as the charge carrier recombination site and undermine the photovoltaic performances of the solar cells. Thus, an interlayer strategy that can effectively separate the direct contact of the electron transport layer and the active layer without impeding the charge transfer is of particular interest.

Here in this work, we report a reductive interlayer based on L-glutathione reduced (L-G, Fig. 1a and 1b) for our semitransparent OPV device. The device uses PM6/Y6 as the active layer (the molecular structures of PM6 and Y6 are shown in Supplementary Fig. 1). Lower interface resistance and facilitated charge transfer between the ZnO layer and the PM6/Y6 active layer is realized by the insert of the interlayer. The PCE of the semitransparent device increases from 11.6% to 13.5%, with an enhancement of *Jsc* from 20.5 to 22.2 mA cm<sup>-2</sup>. Additionally, due to the strong reducibility of the L-G molecule, the production of the radicals is significantly reduced. Density functional theory (DFT) quantum mechanical simulation calculations confirm the defect passivation from the functional groups of the L-G molecules and the superoxide radical suppression effect. After continuous illumination with 1-sun intensity for 500 hours, the molecular structure and packing in the organic active layer remain almost unchanged, while the reference active layer shows a distinct aggregation and decomposition. The semitransparent OPVs with the L-G interlayer maintain over 84% of their initial PCE after 1008-hour continuous illumination. The integration of the resulted semitransparent OPV as the power generating roof shows that the plant growth in the semitransparent OPV-integrated greenhouse is preferable to the one in the traditional glassroof greenhouse with higher survival rate. These results reinforce the feasibility of the semitransparent OPVs in agricultural applications and other practical scenarios.

#### Results

#### Enhanced photovoltaic performances

As shown in Fig. 1b, the basic device architecture for the semitransparent OPVs is ITO/ZnO/ active layer/MoO<sub>3</sub>/ultrathin gold (Au)/ultrathin Ag. The ultrathin layer of Au provides nucleation centers to ensure the formation of a continuous Ag film even with small thickness. A thin L-G interlayer was inserted between the ZnO layer and the active layer via spin-coating and annealing processes. Confirmed by atomic force microscope (AFM) images, the morphologies of the ZnO film surface did not significantly change with the incorporation of the L-G layer (Supplementary Fig. 2 and Extended Data Fig. 1). The J-V curves of the devices with the interlayer showed a significant enhancement of the Jsc (increased from 20.5 mA cm<sup>-2</sup> to 22.2 mA cm<sup>-2</sup>, Fig. 1c). As a result, the averaged PCE of the semitransparent devices increased from 11.6% to 13.5% (other parameters are summarized in **Table 1**). The external quantum efficiency (EQE) spectra confirmed the enhanced Jsc upon the incorporation of the L-G interlayer (Fig. 1d). The transmittance measurements showed similar AVTs of the devices with and without the L-G interlayer, which indicated that the insertion of the interlayer did not influence the transparency of the semitransparent solar cells (Fig. 1e). To evaluate the bifacial properties of the semitransparent devices, we also measured the reflectance and J-V curves of the devices with the interlayer from the Ag side (Supplementary Fig. 3). A PCE of 3.6% with reflectance of 49.1% from 400 nm to 700 nm was obtained (Supplementary Table 1).

We compared the contact resistance of the devices by electrochemical impedance spectroscopy (EIS) measurements. The cell was biased to its open-circuit potential and probed with a low amplitude AC voltage signal. The current was measured for a range of AC frequencies to observe the change of device impedance. We fitted the Nyquist plots of the devices (Fig. 1f) with the equivalent circuit (inset of Fig. 1f). The impedance response of the semitransparent solar cell at low frequencies is related to the recombination resistance,  $R_{rec}$ , and the impedance response at high frequencies is related to the charge transfer resistance, Rt. The results showed that the  $R_{rec}$  values of the semitransparent devices with and without the L-G interlayer are similar (the  $R_{rec}$  without the L-G interlayer is 10.1  $\Omega$  cm<sup>2</sup>, while the  $R_{rec}$  with the L-G soft interlayer is  $10.8 \Omega \text{ cm}^2$ ). In contrast, the  $R_t$  reduced from  $203.4 \Omega \text{ cm}^2$  to  $102.5 \Omega$ cm<sup>2</sup> after the incorporation of the L-G interlayer. This result presents that a much lower charge transfer resistance was obtained by the insertion of the L-G interlayer. We also measured transient photocurrent (TPC) of semitransparent OPVs to further compare the charge carrier extraction of the solar cells with and without the L-G interlayer. The TPC curves exhibited a significantly faster decay for devices with the interlayer (Fig. 1g), indicating a notable enhancement of charge extraction rate. Better charge extraction with less carrier recombination

explains the higher  $J_{SC}$  obtained from the J-V tests. The facilitated charge transport should be attributed to the lower roughness of the ZnO surface with L-G interlayer (Extended Data Fig. 1, from 4.6 nm to 3.3 nm). To further investigate the charge extraction properties of the semitransparent OPVs with and without the L-G interlayer, we measured the photocurrent density ( $J_{Ph}$ ) versus the effective voltage ( $V_{eff}$ ) of the devices (**Fig. 1h**). The value of  $J_{Ph}$  is defined as  $J_L - J_D$ , where  $J_L$  and  $J_D$  are the current densities under illumination and in dark conditions, respectively.  $V_{eff}$  is defined by  $V_0 - V$ , where  $V_0$  is the voltage when  $J_{Ph} = 0$  and  $V_0$  is the applied voltage. At high  $V_{eff}$ , all the photogenerated excitons are dissociated into free charge carriers and collected by electrodes, and the saturation photocurrent density ( $J_{sat}$ ) is only limited by the absorbed incident photons. We obtained a higher  $J_{Ph}/J_{sat}$  of the semitransparent device with the L-G interlayer at low electric field than that of the one without the interlayer. It suggests facilitated charge transfer at the interface between the electron transport layer and the active layer with the L-G interlayer.

#### Simulation elaboration

DFT calculations were carried out to understand the physical mechanism underlying defect passivation effect of L-G interlayer. The computational details and calculation parameters can be found in Methods. We first calculated the defect formation energy (DFE) of the wurtzite ZnO surface and identified the two major defects that are easy to form in the ZnO film, i.e., oxygen vacancy (DFE: 0.27 eV) and zinc interstitial (DFE: 1.05 eV) (Fig. 2a and 2b). The L-G molecule is consisting of three parts: glutamate, cysteine, and glycine (Fig. 2c). We then separately simulated the interaction energy (Inter. Ener.) of each part with the two defects. The cysteine turns out to have a strong interaction with the oxygen vacancy (Inter. Ener.: -4.98 eV) while the glycine interacts tightly with the zinc interstitial (Inter. Ener.: -5.46 eV) (Fig. 2d-f). This indicates that the L-G molecule can effectively nullify both major defects in the ZnO film and reduce the carrier recombination at the interface. The passivation effect of the L-G interlayer is also confirmed by the enhanced internal quantum efficiency (IQE) of the semitransparent device with the L-G interlayer compared to the IQE of the opaque device without the L-G interlayer (Supplementary Fig. 4). Further, we investigated the influence of L-G on the superoxide formation. There is almost no interaction between oxygen molecule and perfect ZnO surface (Supplementary Fig. 5a). However, the oxygen vacancy on ZnO surface can interact with the oxygen molecule and charge transfer occurs from the surface to the oxygen molecule, which is a necessity for superoxide formation (Supplementary Fig. 5b, c). In the presence of the L-G molecule, oxygen is not attracted by the oxygen vacancy since the defect is already nullified by the cysteine part of the L-G (Supplementary Fig. 5d). The charge transfer

from the ZnO surface to the O<sub>2</sub> is impeded by the L-G molecule, avoiding the formation of the superoxide molecule (Supplementary Fig. 5e). Thus, from these simulation results, two different functions of the L-G interlayer can be elaborated. The first one is the defect passivation effect of the L-G interlayer on the ZnO layer. The strong interactions between the L-G molecule and the charge defects on the ZnO surface (i.e., oxygen vacancy and zinc interstitial) can alleviate the charge carrier trapping ability of the defects. The second effect is the superoxide suppression, as the superoxide formation is usually triggered by the oxygen vacancy on the ZnO surface.

#### *Improved operational stability*

To assess the morphological change of the active layer under continuous solar radiation, we compared the grazing-incidence wide-angle X-ray scattering (GIWAXS) patterns of the PM6/Y6 films on ZnO films with and without the L-G interlayer. As shown in Fig. 3a, the 2D GIWAXS patterns are similar prior to continuous radiation. The diffraction peak at q = 1.73 ${\rm \AA}^{-1}$  along the profiles in out-of-plane (OOP) direction was assigned to be the  $\pi$ - $\pi$  stacking of the PM6, the diffraction peak at  $q = 0.29 \text{ Å}^{-1}$  along the in-plane (IP) direction was assigned to be the lamellar stacking of either Y6 or PM6. Upon 500-hour continuous radiation under 1-sun intensity in the air, along the OOP direction the  $\pi$ - $\pi$  stacking peak of the organic film on ZnO layer with the L-G interlayer did not change (Fig. 3b). In contrast, a distinct peak broadening of  $\pi$ - $\pi$  stacking of the film directly deposited on the ZnO layer indicates organic molecular destruction and the morphological alteration of the active layer after the continuous radiation. The 1-D profile of the film on ZnO layer without the L-G interlayer along the IP direction also showed a broadened peak at  $q = 0.29 \text{ Å}^{-1}$  after the continuous radiation, suggesting the breakdown of the lamellar structure (Fig. 3c). Besides, an additional peak at  $q = 0.43 \text{ Å}^{-1}$  showed up at IP direction of the reference sample after the continuous radiation in air. This peak should be attributed to the lamellar packing of the Y6 molecules, and it did not appear in the sample with the L-G interlayer. It indicates that the phase separation was suppressed by the interaction between the active layer and the L-G interlayer (Supplementary Fig. 6). The GIWAXS patterns prove that the incorporation of the L-G interlayer can both suppress the degradation of the active layer and remit the molecular aggregation under continuous radiation. We proceeded to compare the C 1s XPS spectra of the active layer films with and without the L-G interlayer before and after 300-hour continuous radiation (Fig. 4a). The reference film without the interlayer showed a distinct C-O shoulder peak after the exposure, while the spectra of the film with the interlayer remained roughly the same. It experimentally proves that the reductive interlayer successfully impeded the oxidation of the organic molecules in the active layer. The

EPR spectra (Extended Data Fig. 2) shows that the superoxide radical signal greatly reduced under UV radiation with the L-G interlayer. This result manifested the suppression of the superoxide of the L-G molecule, which agrees with the simulation data. To detect the superoxide level inside of the active layer, we further used hydroethidine as the radical trap (HE probe), which can easily react with the superoxide radicals and get transformed into ethidium with different photoluminescence peak positions (Fig. 4b). The superoxide generation rate in the organic active layer rate is distinctly slower with the interlayer, once again confirming the superoxide suppression effect. We further used coumarin (a compound that specifically reacts with hydroxide radical and produce strong luminescence) to investigate the generation rate of the hydroxide radicals of the ZnO films with and without L-G interlayer. The results also showed that the hydroxide radicals were also largely suppressed by the L-G interlayer (Extended Data Fig. 3). The suppressed superoxide and hydroxide radical generation notably led to enhanced operational stability of the encapsulated semitransparent OPVs devices based on PM6/Y6 (Fig. 4c). The devices with the L-G interlayer maintained over 84% of their initial efficiency after 1008-hour exposure under continuous illumination with a metal-halogen xenon lamp source ( $90 \pm 10 \text{ mW cm}^{-2}$ ) at a temperature around 45 °C and relative humidity (RH) about 40% (Fig. 4d). To diminish the influence of morphological change and enhance the light-induced oxidation effect, we tested the unencapsulated devices under 5-sun illumination with temperature of 45 °C and humility about 40%. The results show that the devices with the L-G interlayer maintained about 63% of their initial PCEs while the references completely degraded after 502 hours (Extended Data Fig. 4a). We further tested the thermal stability of semitransparent OPVs with and without the L-G interlayer in inert environment. The ones with the interlayer maintained over 70% of their initial PCEs while the references lost about 95% of the initial PCEs after 502 hours (Extended Data Fig. 4b). It should be attributed to the interactions between the L-G interlayer and the active layer molecules. The interactions alleviated the molecule aggregation and phase separation of the active layer during the stability tests. It is also confirmed by the morphology changes of the active layers on ZnO layer with and without L-G interlayer (Extended Data Fig. 5).

#### Plant growth conditions

To verify the capability to grow various plants in the photovoltaics/photosynthesis integrated system, we built the greenhouses with roofs of the semitransparent OPV devices incorporated with the L-G interlayer and compared the growth conditions of multiple common crops, i.e., mung bean, wheat, and broccoli sprout, in the greenhouses with the ones growing in the greenhouses with roofs of transparent glass and segmented inorganic solar cells (**Fig. 5a** 

and Supplementary Fig. 7, 8). We monitored the growing conditions of the plants for 8 consecutive days under the natural sunlight without a UV filter (Extended Data Fig. 6 to Extended Data Fig. 8). As shown in Fig. 5b to 5d, we summarized the sprout lengths, length deviations, biomass productivities, and survival rates of the plants after 8-day growth as the parameters of the evaluation. Since the wheat sprouts do not have leaves, we only included the leave area data for the mung bean and hearty broccoli. Both the sprout lengths and survival rates of the plants grown in the greenhouses with semitransparent OPV roofs are comparable/higher than the ones grown in the greenhouses with transparent glass or spatially segmented inorganic solar cell roofs. The higher survival rates should be attributed to the UVlight absorbing properties of the roofs that fully covered with semitransparent OPV as the UV exposure undermines the biological activity of the sprouts.<sup>27-29</sup> To confirm this, we also integrated a UV filter over the greenhouses during another batch of plant growth. As shown in Supplementary Fig. 9, the height, number of the branches, and the leave area of the sprouts grew under the transparent glass roof were quite comparable to (or slightly higher than) the ones in the greenhouse with the semitransparent OPV roof. The results indicate that the integration of the semitransparent OPVs as the greenhouse roof will not impair the growth of the plants (by competing for the sunlight absorption). Interestingly, the semitransparent OPV roof will protect the plants from the detrimental UV exposure and promote the growth of the plants in the greenhouses. The photovoltaic and photosynthesis integration can be achieved with reciprocity. The biomass productivity together with the concurrent electricity production of the system are estimated in Supplementary Table 2. Combined with the elongated operational lifetime of the semitransparent OPVs with the L-G interlayer, successful commercialization of environmentally friendly greenhouses is expected.

#### Discussion

Aiming to resolve the stability issue of the semitransparent OPVs with an agricultural application, we introduced a reductive interlayer into the device architecture. The charge carrier extraction and transportation were enhanced due to the nullification of the charged charger traps in the ZnO layer. The insertion of the L-G interlayer led to an improved averaged PCE of 13.5% while maintaining the AVT of the semitransparent devices. The suppression of the superoxide generation was observed under the radiation. As a result, the PCE of the devices with the L-G interlayer maintained over 84% after continuous illumination for 1008 hours. Greenhouse roofs using the semitransparent OPV devices have guaranteed the thriving growth of various plants with higher survival rates. Our study highlights the importance of operational

stability of organic photovoltaics and the reciprocity of the photovoltaic and photosynthesis integration.

#### Methods

#### Materials

All chemicals were obtained commercially and used without further purification. The polymer donor PM6 (the full name is poly[(2,6-(4,8-bis(5-(2-ethylhexyl-3-fluoro)thiophen-2-yl)benzo[1,2-b:4,5-b']dithiophene))-alt-(5,5-(1',3'-di-2-thienyl-5',7'-bis(2ethylhexyl)benzo[1',2'-c:4',5'-c']dithiophene-4,8-dione)]) and acceptor Y6 (the full name is 2,20-((2Z,20Z)-((12,13-bis(2-ethylhexyl)-3,9-diundecyl-12,13-dihydro-[1,2,5]thiadiazolo[3,4-e]thieno[2,"30':4',50] thieno[20,30:4,5]pyrrolo[3,2g]thieno[20,30:4,5]thieno[3,2-b]indole-2,10-diyl)bis(methanylylidene)) bis(5,6-difluoro-3oxo-2,3-dihydro-1H-indene-2,1-diylidene))dimalononitrile) were purchased from Solarmer Inc. (Beijing, China). 1 chloronaphthalene (CN), and chloroform (CF) were obtained from Sigma-Aldrich Inc. (St. Louis, United States). For interlayer, L-glutathione reduced (L-G) and pure water were purchased from Sigma-Aldrich Inc. (St. Louis, United States). For the transport layers, zinc oxide (ZnO) nanoparticle solution and molybdenum trioxide (MoO3) powder were also purchased from Sigma-Aldrich Inc. (St. Louis, United States). Coumarin (COU) was purchased from Alfa Aesar Co., Ltd..

#### Solar cell fabrication

Organic solar cells were fabricated with the following structure: indium tin oxide (ITO)/zinc oxide (ZnO)/active layer/molybdenum trioxide (MoO<sub>3</sub>)/silver (Ag) (various thickness). The ITO glass was pre-cleaned in an ultrasonic bath of acetone and isopropanol, and treated in ultraviolet-ozone chamber (Jelight Company, USA) for 10 min. A thin layer (30 nm) of ZnO sol-gel was spin-coated onto the ITO glass and baked at 200 °C for 60 min. To obtain the active layers, a mixture of PM6/ Y6 (7:9, w/w) dissolved in CN/CF (0.5%, v/v) mix solvent with stirring for 1.5 h (60 °C). Then, the blend solutions were separately spin-coated on the ZnO layer to form the photosensitive layers. The thickness of active layer was 90-110 nm. A MoO<sub>3</sub> (ca. 10 nm) and Ag layer (100 nm for opaque devices, 15 nm for semitransparent OPVs) was then evaporated onto the surface of the photosensitive layer under vacuum (ca. 10<sup>-5</sup> Pa) to form the back electrode. The active area of the device was 0.12 cm<sup>2</sup>. For semitransparent OPVs, a 1 nm gold (Au) layer was evaporated between MoO<sub>3</sub> and Ag. The L-G interlayer was applied by spin coating solution with L-G dissolved in pure water (1.5 mg ml<sup>-1</sup>) onto the ZnO layer. The solution (20 μL) was driped on the ZnO layer surface after the substrate reached and kept at

4000 rpm. The spinning was stopped in 10 seconds and the substrate was immediately moved to the hot place and baked at 95 °C for 3 min in the nitrogen glovebox. The device encapsulation was conducted in nitrogen atmosphere by using glass slits and UV curable sealant (Norland Optical Adhesives 60). We covered the glass slits with the adhesive and put them on the metal electrode side of the organic solar cell devices. A UV lamp (UVP Analytik Jena) was used for adhesive curing for 10 seconds at a distance about 3 cm with an intensity of about 5 mW cm<sup>-2</sup>.

#### Device characterization

Current-voltage (*J-V*) characterizations of the solar cells were carried out with Keithley 2401 source meter, under simulated one sun illumination (AM 1.5G, 100 mW cm<sup>-2</sup>) (Oriel Sol3A with class AAA solar simulator, Newport). The intensity calibration of the light was done by NREL-certified Si photodiode with a KG-5 filter. The measurement of solar cells was carried out in an ambient atmosphere without pre-conditioning such as voltage bias and light soaking and a scan rate of 0.1 V s-1 (-1.0 V to 1.0 V) was used for *J-V* characterizations with a mask with area of 0.1 cm<sup>2</sup>.

The incident photon-to-electron conversion efficiency (IPCE) measurement was carried out by using specially designed system (Enli tech) under AC mode (chopping frequency: 133 Hz) without bias light. The system integrates all optical and mechanical components inside 60cm x 60cm x 60cm main body which includes electrical signal acquisition lock-in amplifiers. The lamp wavelength range is from 250 nm to 2500 nm (Xe75). A Si diode (RC-S103011) was used for calibration before the measurements. The devices were measured in dark using a 3M clip (923690-14). Electrochemical impedance spectroscopy (EIS) measurements were conducted with an electrochemical workstation (Zennium Zahner, Germany) with a 20-mV amplitude for AC perturbations ranging from 100 mHz to 1 MHz. The transmittance spectra of the semitransparent OPVs were obtained using a U-4100 spectrophotometer (Hitachi) equipped with integrating sphere, in which monochromatic light was incident to the substrate side. For transient photocurrent (TPC) measurements, a white light bias was generated from an array of diodes (Molex 180081-4320) to simulate 0.5 sun bias light working condition. A pulsed laser (510 nm) pumped by a nitrogen laser (LSI VSL-337ND-S) was used as the perturbation source, with a pulse width of 3 ns and a repetition frequency of 3 Hz. The intensity of the perturbation laser pulse was controlled to maintain the amplitude of transient V<sub>OC</sub> below 5 mV so that the perturbation assumption of excitation light holds. The currents under short circuit conditions were measured over a 50  $\Omega$  resistor and were recorded on a digital S4 oscilloscope (Tektronix DPO 4104B).

#### Film characterization

Grazing-incidence wide-angle X-ray scattering (GIWAXS) measurement was performed at Advanced Light Source on the 7.3.3. beamline. All samples were deposited on the silicon wafer with 100 nm silicon oxide. Samples were irradiated by 10 keV at a fixed X-ray incident angle of 0.10°-0.14° with an exposure time of 3 s. X-ray Photoelectron Spectroscopy (XPS) measurements were carried out on an XPS AXIS Ultra DLD (Kratos Analytical). An Al Ka (1,486.6 eV) X-ray was used as the excitation source. A high-resolution Jordan Valley D1 X-ray diffractometer with Cu Kα radiation and incident parallel beam optics was employed to obtain the ω:2θ scans. For superoxide probe measurements, 31.7 μM solution of the hydroethidine probe was prepared by dissolving 10 mg in 10 ml of dry toluene, followed by sonication to facilitate miscibility. The active layer films were then added to 10 ml of 0.317 μM solution created from the stock solution. Photoluminescence spectra were recorded using an excitation wavelength of 520 nm and slit widths of 10 mm on a Horiba Yobin-Ybon Fluorolog-3 spectrofluorometer. For hydroxide probe measurements, ZnO films with and without L-G interlayer was dispersed in 10 mL of 10<sup>-3</sup> M COU aqueous solution in a dish with a diameter of about 7.0 cm. A 350W Xenon arc lamp (Ushio America, Inc.) was used as a light source. The average light intensity striking on the surface of the reaction solution was about 5.0 mW cm<sup>-2</sup>, as measured by a UV radiometer (Model: Rejuvenate UVoT UV HVAC Monitor System) with the peak intensity of 365 nm. Fluorescence spectra of generated 7hydroxycoumarin was measured on a Hitachi Fluorolog-3 fluorescence spectrophotometer. The excitation wavelength was 332 nm.

#### Computational method

All surface calculations for ZnO layer were performed using plane-wave based Density Functional Theory (DFT). The 5x5x2 ZnO slabs were generated along the wurtzite [001] direction and a 10-15 Å vacuum slab were added. For all geometry optimizations and self-consistent field calculations Perdew-Burke-Ernzerhof type generalized gradient approximation (GGA-PBE) for the exchange-correlation functional with a 300eV plane-wave cutoff and 4x4x1 k-point mesh for Brillouin zone sampling were chosen.<sup>30</sup> Dispersion corrections to electronic energies based on Grimme's DFT-D3(BJ) scheme were included.<sup>31,32</sup> Ionic positions and volumes were relaxed using a conjugate gradient algorithm, until all residual forces are smaller than 0.01 eV Å<sup>-1</sup>. First-principles calculations were performed based on the density functional theory (DFT) using a plane-wave basis set and the projected augmented wave (PAW) method, as implemented in the VASP package.<sup>33,34</sup>

Defect formation energies are predicted using the following formula:

$$\Delta H_D^q = E_D^q - E_0 + \sum_i \Delta n_i \mu_i$$

where D and q denotes the defective energy and charge states, respectively.  $E_0$  is the non-defective energy,  $\Delta n_i$  is the number change in element removal (or addition) to create defect and  $\mu_i$  is the corresponding chemical potential.  $E_F$  is the Fermi energy and  $E_{VBM}$  is the valence-band maximum energy.

Defect-molecule interaction energies were predicted using the expression:  $E_{int} = E_{d,m} - [E_d + \mu_m]$ , where  $E_{d,m}$  is the total energy of the supercell containing the defect plus molecule,  $E_d$  is the total energy of the system with the defect only and  $\mu_m$  is the chemical potential of the molecule.

Charge-density difference (CDD)

$$\Delta \rho = \rho_{comp} - \rho_{sur.} - \rho_{mol}$$

is calculated to quantify the charge-transfer between the defect and the molecule, where  $\rho_{comp}$ ,  $\rho_{surf}$  and  $\rho_{mol}$  are the three-dimensional charge density distributions of the defective surface-molecule complex, defective surface, and free molecule, respectively.

#### EPR measurements

Electron spin resonance (ESR) measurements were performed on a Bruker EMXPlus ESR spectrometer equipped with a TE011 microwave cavity ER 4119HS. Before the EPR measurements, OPV samples with and without L-G layer were placed in a 50 mM solution of 5,5-dimethyl-1-pyrroline-N-oxide (DMPO) obtained from Sigma-Aldrich Inc. in a solution of anhydrous dimethyl sulfoxide (DMSO) purchased from Sigma-Aldrich Inc.. Samples were drawn into open-ended polytetrafluoroethylene (PTFE-ID: AWG21) tubing bought from Zeus. The tubing was then folded in half, and the open ends were squeezed by the pliers. After folding, the tubing was then placed into a quartz tube made by Wilmad Glass Co, which was placed in the ESR cavity. The EPR spectra represent the average of five runs and were acquired employing a sweep time of 10 s, microwave frequency of 9.297431 GHz, microwave power of 6.3 mW, sweep width of 80 G, and modulation amplitude of 1 G. After taking an ESR spectrum without UV illumination, the sample was taken out of the cavity and illuminated with a UVG-54 handheld UV lamp – 254 nm 6 W – for 5 minutes. Then, the sample was promptly put in the cavity and measured again. The ESR signal of the DMPO–O2• adduct has a characteristic spectrum<sup>35</sup>, Extended Data Fig. 2.

#### Plant growth in greenhouses with different roofs

#### *Greenhouse assembly*

Transparent plexiglass sheets (Sosco Metals) were used to build the greenhouse framework with a length of 30 cm, a width of 21.5 cm, and a height of 15 cm. Semitransparent organic solar panels, opaque organic solar panels, segmented inorganic solar panels, and transparent panels were studied. Each greenhouse has two roofs with a length of 30 cm, a width of 15 cm, and 45 degrees toward the horizon. To ensure complete coverage of the solar cells between the lighting and plant, the walls of each greenhouse are covered by the black tape and aluminum foil during the plant growth. Rectangular polypropylene trays (SHEING) with a length of 26.5 cm and a width of 19.5 cm were used to germinate the plants and were placed directly under the greenhouse. When verifying the influence of the UV light on the plant growth, we added an extra UV filter (Edmund Optics) on the top of the greenhouse roofs.

#### Plant growth condition measurement

Three types of commonly consumed plants, mung bean, wheat, and broccoli sprout, were chosen to evaluate the growing condition under greenhouses with different roofs. Depending on the size of their seeds, the seed spacings for mung bean, wheat, and broccoli sprouts were 0.2 count cm<sup>-2</sup>, 0.3 count cm<sup>-2</sup>, and 2.7 count cm<sup>-2</sup>, respectively. All seeds were immersed in water for 1 day before placed evenly in a tray with water underneath. Then, each tray was loaded with a different greenhouse and placed outside for eight consecutive days. The water temperature in the greenhouses was kept stable by changing it with fresh water (~20 °C) every hour during daytime. The environmental conditions of the plant growth were summarized in Supplementary Table 3 to Supplementary Table 5. The height of the plants was monitored daily at 6 PM, together with water refilling to ensure the plants stayed hydrated. The length of the sprouts was measured based on the distance from the top to the beginning of the root. The area of the leaves was collected by taking off the leaves and analyzing them using Image J. The survival rate was calculated by counting the number of surviving sprouts normalized by the number of initial seeds. All the plants in the different greenhouses were counted and averaged for statistical analysis.

#### Biomass productivity calculation

To evaluate the plant biomass productivity, we measured the biomass of the different crops after growing in the greenhouses for eight days. We measure the biomass by summing the dry

mass of all organics, including the surviving sprout, the roots, dead sprouts, and ungerminated seeds. We placed them in an 90°C oven for three days to remove excess water.<sup>36</sup> The weight of each batch was measured using a balance, and the final weight was normalized based on their initial mass for the convenience of comparison. Then we calculate the biomass productivity by using the following equation:<sup>37-39</sup>

$$P = (N_2 - N_1)/(t_2 - t_1)$$

where  $N_1$  and  $N_2$  are defined as the biomass at time 1 ( $t_1$ ) and time 2 ( $t_2$ ), respectively. Concurrent electricity production estimation

Global horizontal irradiance (GHI) is the total solar radiation incident on a horizontal surface. It is the sum of direct normal irradiance (DNI), diffuse horizontal irradiance, and ground-reflected radiation. GHI used to evaluate the concurrent electricity production was provided by Solcast. Local cloud covering was included to render a precise and accurate global snapshot of solar irradiance. The GHI data at UCLA every 60 min and is summarized in Supplementary Table 3 to Supplementary Table 5. The total energy power and the daily average power for each round of plant growth were calculated based on the GHI profile. Considering the performance loss during scaling up, we used 20% and 11% as the power conversion efficiencies for inorganic solar cells and semitransparent solar cells in the estimation. The electricity production for each greenhouse was calculated based on the roof panel size, the angle to the horizon, and the GHI profile.

#### Data availability

All relevant data that support the findings of this study are presented in the article and Supplementary Information. Source data are available from the corresponding authors upon reasonable request.

#### **Acknowledgments**

This work is supported by the California Energy Commission (Grant No. EPC-19-002). Computing resources used in this work were provided by the National Center for High Performance Computing (UHEM) of Turkey (Grant No. 1008342020). C.D. would like to thank the Fulbright Turkey Commission for providing a valuable scholarship for his post-doctoral study at the United States. M.H. acknowledges financial support from the National Natural Science Foundation of China (NSFC) (Grant Nos. 12104081, 51872036) and China

Postdoctoral Science Foundation (Grant No. 2022T150087). M. P. acknowledges financial support from National Science Foundation Research in Undergraduate Institutions (RUI) (Grant No. 1856746).

#### **Author contributions**

Y. Z. and Y. Y. conceived the idea. Y. Z. conducted the experiments, and prepared the manuscript under the supervision of Y. Y.. C. D. and I. Y. performed the DFT calculations. Z. L. prepared the samples for EQE, GIWAX, and XPS measurements. Z. L. collected GIWAX data of the films. M. P. conducted the EPR measurements. Q. X. helped with the XPS measurements. M.W. collected EIS and TPC data under the supervision of J. B.. Z. L. and X. W. built the PV-integrated greenhouses and did the correlated plant observation under the sunlight. B. C. and E. G. S. and helped with the estimation of the biomass productivity and the concurrent electricity production under the supervision of K.-H. W.. W. Y., Y. Z., D. M., E. Z., R. Z., and K. N. H. provided helpful discussion during the project and revised the manuscript. All the authors discussed the results and commented on the manuscript.

#### **Competing interests**

Authors declare no competing interests.

#### **Table**

**Table 1.** Photoelectric performances and the stability under continuous 1-sun illumination of semitransparent OPVs based on PM6/Y6 with and without the L-G interlayer.\*

Condition (PM6/Y6)	Voc (V)	Jsc (mA cm <sup>-2</sup> )	FF (%)	PCE (%)	AVT (%)	PCE retaining after 1008 hours (%)
Semitransparent OPV without L- G interlayer	0.84 ± 0.01	$20.5 \pm 0.2$	67.2 ± 0.3	11.6 ± 0.4	21.2 ± 0.3	$18.4 \pm 6.0$
Semitransparent OPV with L-G interlayer	$\begin{array}{c} 0.86 \pm \\ 0.01 \end{array}$	$22.2 \pm 0.3$	$70.4 \\ \pm 0.4$	13.5 ± 0.4	21.5 ± 0.3	$84.8 \pm 3.7$

<sup>\*</sup> *Voc*: open-circuit voltage; *Jsc*: short-circuit current; *FF*: fill factor; PCE: power conversion efficiency; AVT: averaged visible transmittance.

#### Figure Legends

### Fig. 1: Facilitated charge extraction and enhanced photovoltaic performances by the incorporation of L-G interlayer.

**a**, Molecular structures of L-glutathione reduced. **b**, Device architecture of semitransparent OPVs with L-G interlayer. **C**, J-V curves, **d**, EQE spectra, and **e**, transmittance measurements of the devices with and without the L-G interlayer. **f**, Nyquist plots (inset: the equivalent circuit), **g**, TPC curves, and **h**, photocurrent data as a function of the potential difference  $V_0-V$  of the devices with and without the L-G interlayer.

#### Fig. 2: Interactions between the L-G molecule and the defects on ZnO surface.

**a**, Oxygen vacancy and **b**, zinc interstitial defects on the ZnO surface. **c**, Three parts of L-Glutathione: glutamate, cysteine, and glycine. Interaction energies of oxygen vacancy and zinc interstitial defects with **d**, glutamate, **e**, cysteine, and **f**, glycine part of L-Glutathione.

#### Fig. 3: Morphological stability of the active layer on the L-G interlayer.

**a**, 2D GIWAXS patterns of the PM6/Y6 films on ZnO films with and without the L-G interlayer before and after illumination under 1-sun intensity for 500 hours, and corresponding 1D GIWAXS profiles in **b**, out-of-plane and **c**, in-plane direction (incident angle: 0.13°).

### Fig. 4: Impedance of the organic molecule oxidation by L-G interlayer and enhanced device stability.

**a**, C 1s XPS spectra of the active layer films with and without the L-G interlayer before and after 300-hour continuous radiation. **b**, Reaction that the hydroethidine transforms into ethidium the superoxide radicals. **c**, Normalized fluorescence intensity of the HE probe as a function of illumination time under AM1.5G illumination conditions.  $I_F(t)$  is the fluorescence maximum at time t and  $I_F(t_0)$  is the background fluorescence intensity.  $I_F(t)/I_F(t_0)$  corresponds to the yield of superoxide generation. **d**, PCE changes of the devices with and without L-G interlayer during 1008-hour exposure under continuous illumination.

#### Fig. 5: Plant growth in the photovoltaics/photosynthesis integrated system.

**a**, Scheme of the power-generating greenhouse with semitransparent OPV roof, and plant growth conditions of **b**, mung bean, **c**, wheat, and **d**, broccoli. Biomass among different plant

is normalized into the final mass with 1 g initial seed mass. Survival count is normalized into the number of survived plants per 100 initial seeds.

### Extended Data Fig. 1: Surface morphology of the ZnO layer with and without L-G interlayer.

AFM images of the ZnO surface **a**, without and **b**, with the L-G interlayer, and three-dimensional AFM images of ZnO films **c**, without and **d**, with L-G interlayer.

### Extended Data Fig. 2: Suppression of superoxide radical generation with the L-G interlayer.

EPR spectra of the ZnO films **a**, without and **b**, with the L-G interlayer.

## Extended Data Fig. 3: Suppression of hydroxide radical generation with the L-G interlayer.

**a**, Reaction that the coumarin transforms into 7-hydroxycoumarin by reacting with hydroxide radicals. **b**, PL intensity change at 456 nm of the solution immersed with ZnO films with and without L-G interlayer.

#### Extended Data Fig. 4: Light and heat stability enhancements of unencapsulated devices.

**a**, PCE changes of the devices with and without L-G interlayer during 502-hour exposure under 5-sun continuous illumination. **b**, PCE changes of the devices with and without L-G interlayer during 502-hour heating in nitrogen glovebox.

#### Extended Data Fig. 5: Morphological stability of the active layers on ZnO surfaces.

AFM images of the PM6/Y6 active layers on the ZnO surfaces **a**, **c**, without and **b**, **d**, with the L-G interlayer before and after heating in the nitrogen glovebox for 500 hours.

Extended Data Fig. 6: Growth condition of the mung bean in the greenhouses with roofs of spatially segmented inorganic solar cell, semitransparent OPV, and transparent glass.

Extended Data Fig. 7: Growth condition of the wheat in the greenhouses with roofs of spatially segmented inorganic solar cell, semitransparent OPV, and transparent glass.

Extended Data Fig. 8: Growth condition of the broccoli in the greenhouses with roofs of spatially segmented inorganic solar cell, semitransparent OPV, and transparent glass.

#### References

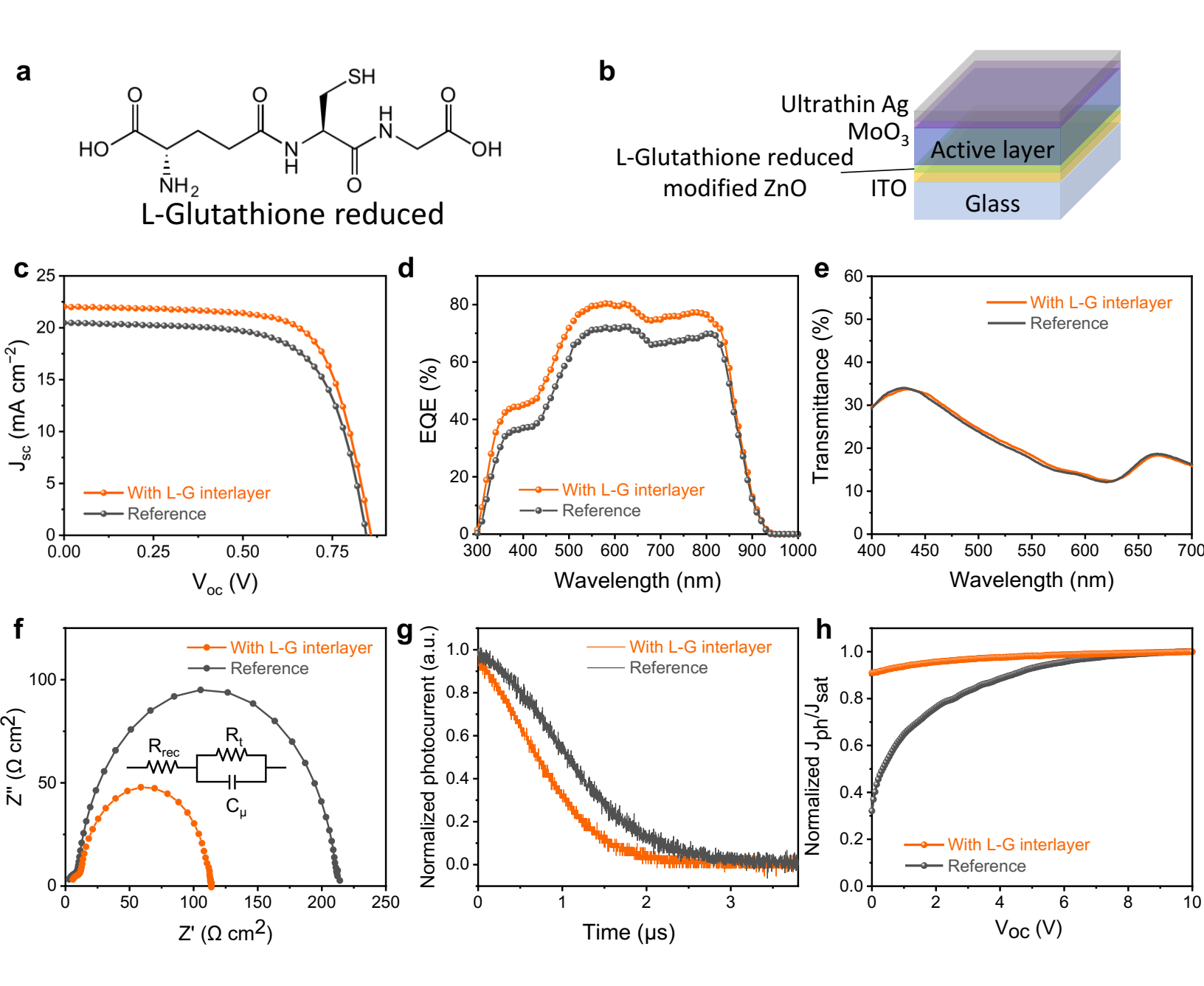
- Wu, A., Hammer, G. L., Doherty, A., von Caemmerer, S. & Farquhar, G. D. Quantifying impacts of enhancing photosynthesis on crop yield. *Nat. Plants* **5**, 380–388 (2019).
- Joshi, S. *et al.* High resolution global spatiotemporal assessment of rooftop solar photovoltaics potential for renewable electricity generation. *Nat. Commun.* **12**, 1–15 (2021).
- Ballif, C., Perret-Aebi, L.-E., Lufkin, S. & Rey, E. Integrated thinking for photovoltaics in buildings. *Nat. Energy* **3**, 438–442 (2018).
- 4 Li, G., Zhu, R. & Yang, Y. Polymer solar cells. *Nat. Photonics* **6**, 153–161 (2012).
- Hou, J., Inganäs, O., Friend, R. H. & Gao, F. Organic solar cells based on non-fullerene acceptors. *Nat. Mater.* **17**, 119–128 (2018).
- 6 Chang, S.-Y., Cheng, P., Li, G. & Yang, Y. Transparent polymer photovoltaics for solar energy harvesting and beyond. *Joule* **2**, 1039–1054 (2018).
- Betancur, R. *et al.* Transparent polymer solar cells employing a layered light-trapping architecture. *Nat. Photonics* **7**, 995–1000 (2013).
- 8 Traverse, C. J., Pandey, R., Barr, M. C. & Lunt, R. R. Emergence of highly transparent photovoltaics for distributed applications. *Nat. Energy* **2**, 849–860 (2017).
- Wang, D. *et al.* High-performance and eco-friendly semitransparent organic solar cells for greenhouse applications. *Joule* **5**, 945–957 (2021).
- Li, Y. *et al.* Color-neutral, semitransparent organic photovoltaics for power window applications. *Proc. Natl. Acad. Sci.* **117**, 21147–21154 (2020).
- Wang, D. *et al.* High-Performance Semitransparent Organic Solar Cells with Excellent Infrared Reflection and See-Through Functions. *Adv. Mater.* **32**, 2001621 (2020).
- Li, Y. *et al.* High efficiency near-infrared and semitransparent non-fullerene acceptor organic photovoltaic cells. *J. Am. Chem. Soc.* **139**, 17114–17119 (2017).
- Ravishankar, E. *et al.* Achieving Net Zero Energy Greenhouses by Integrating Semitransparent Organic Solar Cells. *Joule* **4**, 490–506 (2020).
- 14 Kaltenbrunner, M. et al. Ultrathin and lightweight organic solar cells with high flexibility. Nat. Commun. 3, 1–7 (2012).
- Burlingame, Q., Ball, M. & Loo, Y.-L. It's time to focus on organic solar cell stability. *Nat. Energy* **5**, 947–949 (2020).
- Burlingame, Q. *et al.* Intrinsically stable organic solar cells under high-intensity illumination. *Nature* **573**, 394–397 (2019).
- GhasemM . *et al.* A molecular interaction—diffusion framework for predicting organic solar cell stability. *Nat. Mater.* **20**, 525–532 (2021).
- Deschler, F. *et al.* The effect of ageing on exciton dynamics, charge separation, and recombination in P3HT/PCBM photovoltaic blends. *Adv. Funct. Mater.* **22**, 1461–1469 (2012).
- Jiang, Y. *et al.* Photocatalytic effect of ZnO on the stability of nonfullerene acceptors and its mitigation by SnO 2 for nonfullerene organic solar cells. *Mater. Horiz.* **6**, 1438–1443 (2019).

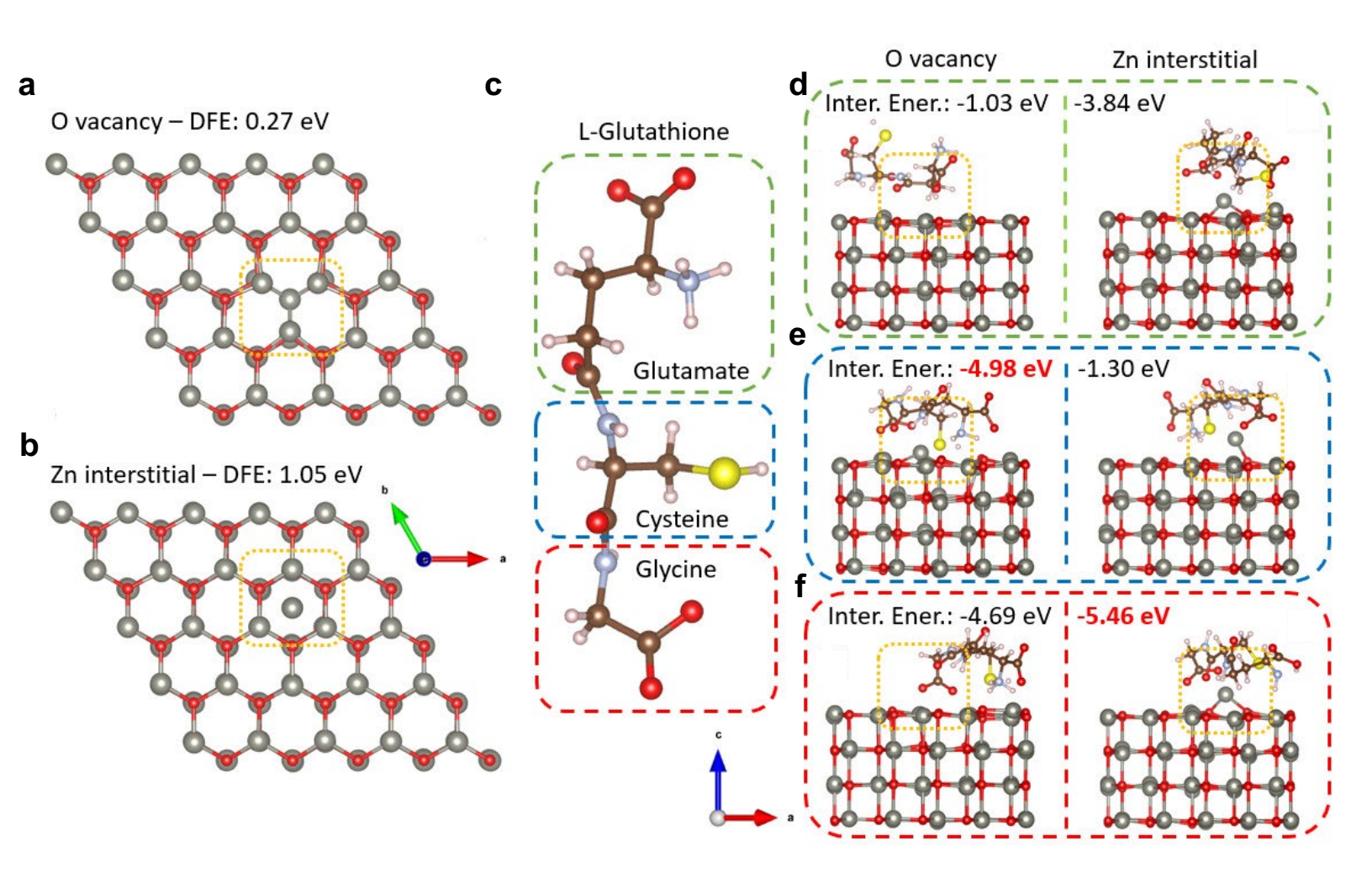
- Li, Y. *et al.* Non-fullerene acceptor organic photovoltaics with intrinsic operational lifetimes over 30 years. *Nat. Commun.* **12**, 1–9 (2021).
- Duan, L. & Uddin, A. Progress in stability of organic solar cells. *Adv. Sci.* 7, 1903259 (2020).
- Hoke, E. T. *et al.* The role of electron affinity in determining whether fullerenes catalyze or inhibit photooxidation of polymers for solar cells. *Adv. Energy Mater.* **2**, 1351–1357 (2012).
- Luke, J. *et al.* Twist and degrade—impact of molecular structure on the photostability of nonfullerene acceptors and their photovoltaic blends. *Adv. Energy Mater.* **9**, 1803755 (2019).
- Gokulnath, T. *et al.* A wide-bandgap  $\pi$ -conjugated polymer for high-performance ternary organic solar cells with an efficiency of 17.40%. *Nano Energy* **89**, 106323 (2021).
- Jiang, H. *et al.* Passivated metal oxide n-type contacts for efficient and stable organic solar cells. *ACS Appl. Energy Mater.* **3**, 1111–1118 (2019).
- Palilis, L. C. *et al.* Inorganic and hybrid interfacial materials for organic and perovskite solar cells. *Adv. Energy Mater.* **10**, 2000910 (2020).
- 27 Larson, R. A. & Berenbaum, M. R. Environmental phototoxicity. *Environ. Sci. Technol.* 22, 354–360 (1988).
- Mackerness, S. A.-H. Plant responses to ultraviolet-B (UV-B: 280–320 nm) stress: What are the key regulators? *Plant Growth Regul.* **32**, 27-39 (2000).
- 29 Caldwell, M. Physiological plant ecology I. (Springer, 1981).

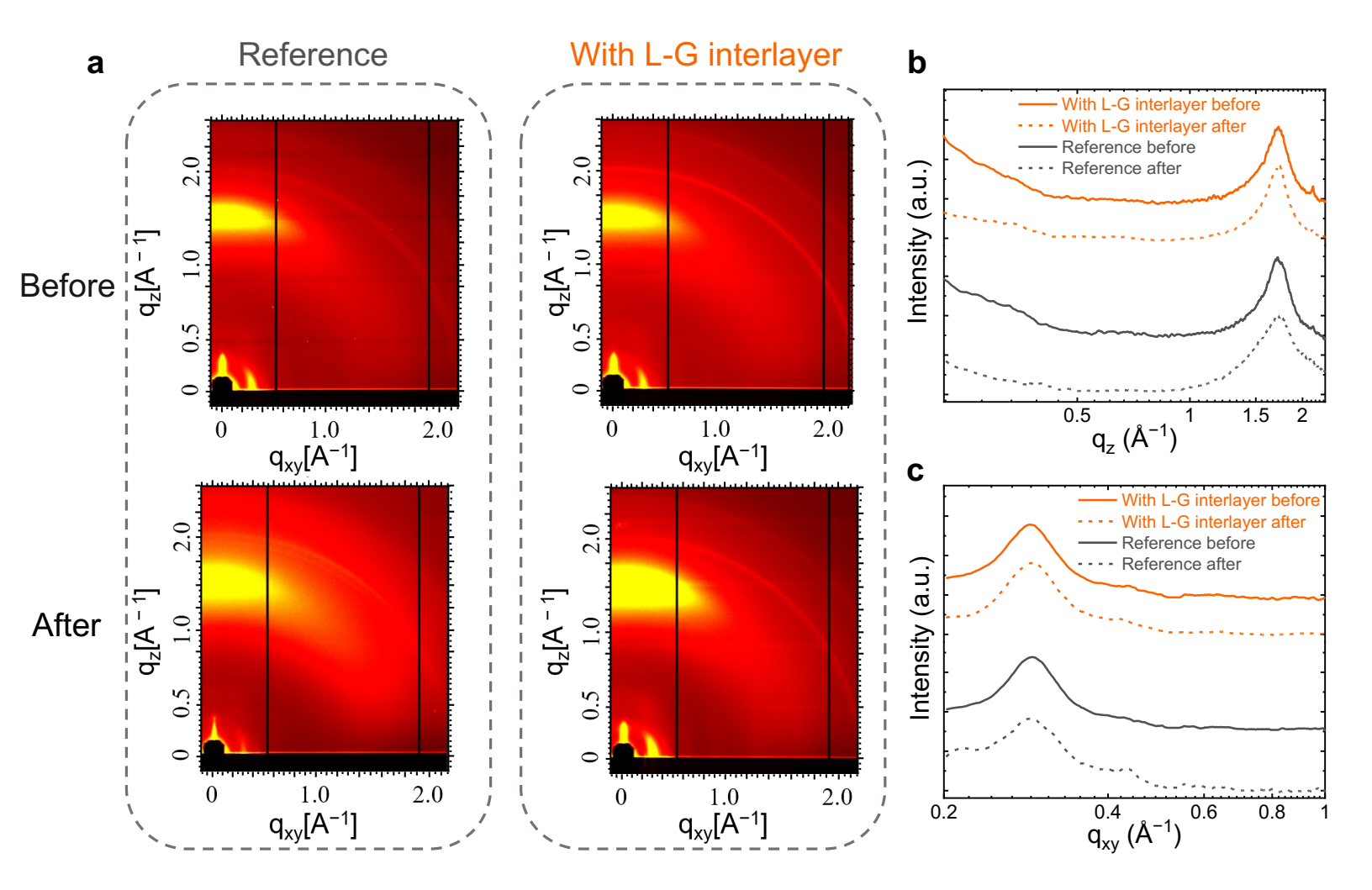
#### **Methods-only references**

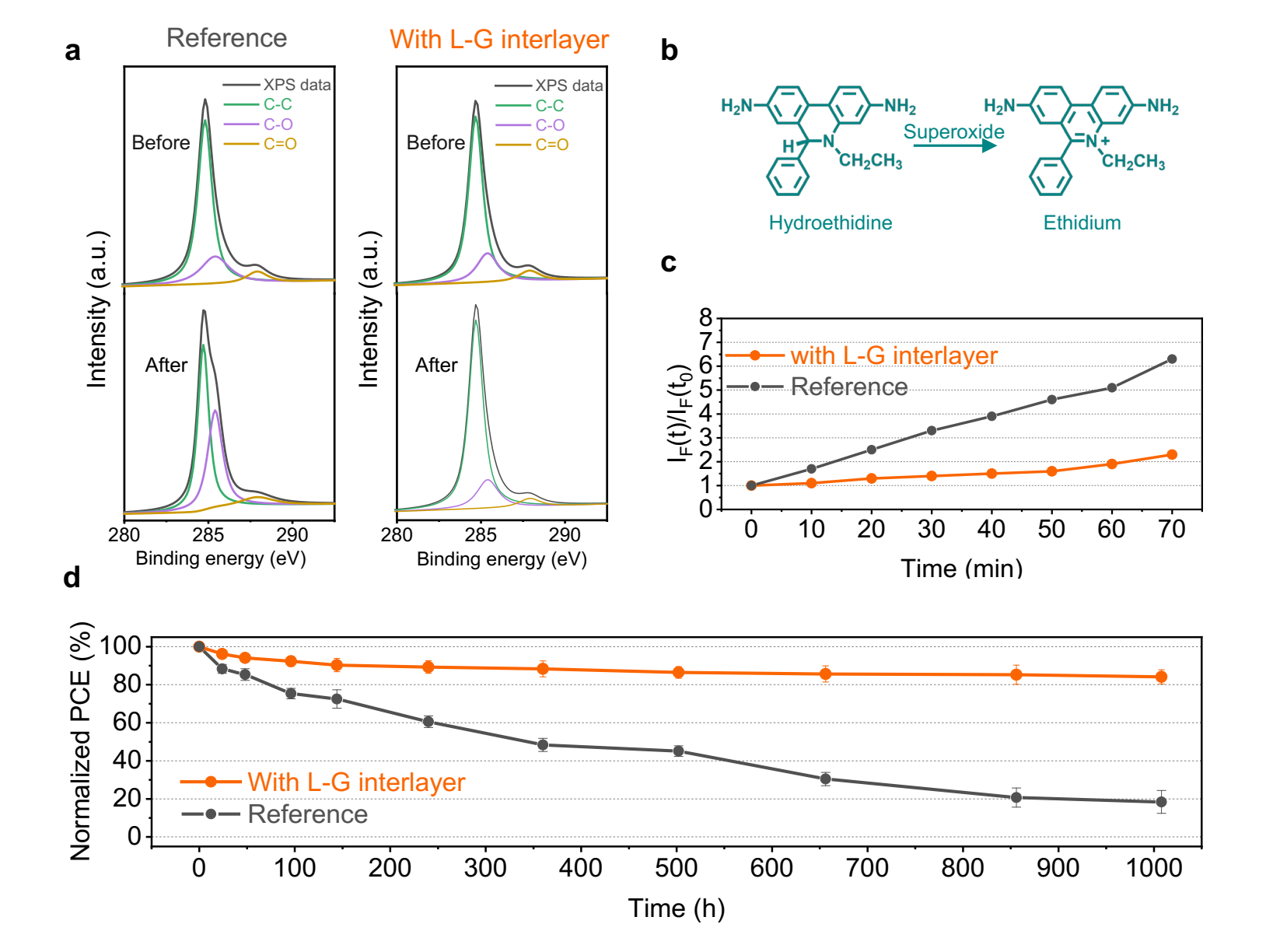
- 30. J. P. Perdew, K. Burke, M. Ernzerhof, Generalized Gradient Approximation Made Simple. *Phys. Rev. Lett.* 77, 3865–3868 (1996).
- 31. J. P. Perdew, A. Ruzsinszky, G. I. Csonka, O. A. Vydrov, G. E. Scuseria, L. A. Constantin, X. Zhou, K. Burke, Restoring the density-gradient expansion for exchange in solids and surfaces. *Phys. Rev. Lett.* **100**, 136406 (2008).
- 32. S. Grimme, Semiempirical GGA-Type Density Functional Constructed with a Long-Range Dispersion Correction, *J. Comp. Chem.* **27**, 1787–1799 (2006).
- 33. G. Kresse, J. Furthmüller, Efficiency of ab-initio Total Energy Calculations for Metals and Semiconductors Using a Plane-Wave Basis Set. *Comput. Mater. Sci.* **6**, 15–50 (1996).
- 34. G. Kresse and J. Furthmüller. Efficient Iterative Schemes for ab initio Total-Energy Calculations Using a Plane-Wave Basis Set. Phys. Rev. B, **54**, 11169 (1996).
- 35. L. Y. Zang, H. P. Misra, EPR kinetic studies of superoxide radicals generated during the autoxidation of 1-methyl-4-phenyl-2,3-dihydropyridinium, a bioactivated intermediate of parkinsonian-inducing neurotoxin 1-methyl-4-phenyl-1,2,3,6-tetrahydropyridine. *J. Biol. Chem.* 267, 23601–23608 (1992).

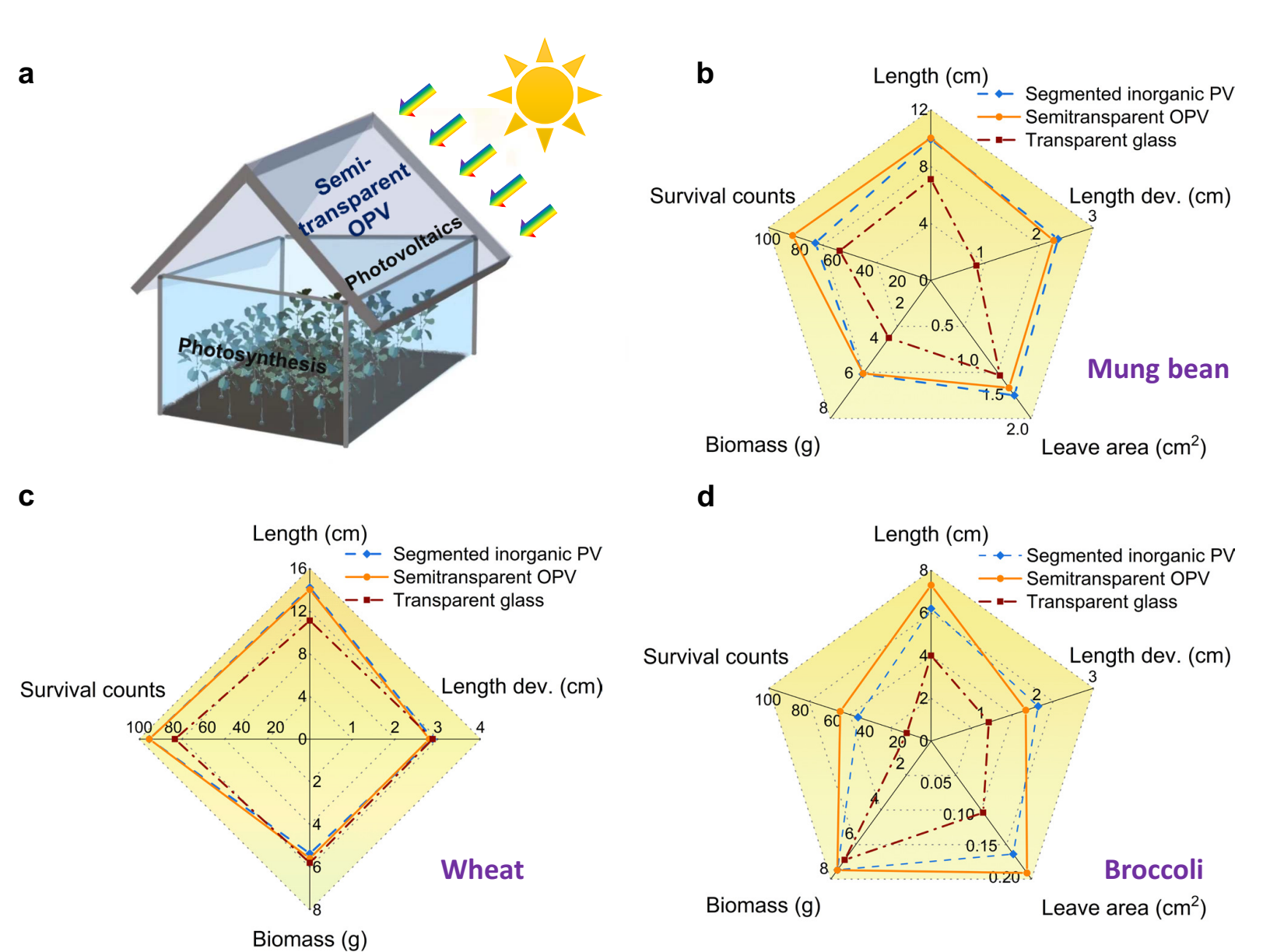
- 36. M. Maldonado, M. Ribes, & F. C. van Duyl, Nutrient fluxes through sponges: biology, budgets, and ecological implications. *Adv. Mar. Biol.*, 62, 113–182 (2012).
- 37. H. E. Young, Biomass production in terrestrial ecosystems. *Microbial Energy Conversion* (pp. 45-58), Pergamon (1977).
- 38. J. Zhu, W. Chen, H. Chen, X. Zhang, C. He, J. Rong, Q. Wang, Improved productivity of neutral lipids in Chlorella sp. A2 by minimal nitrogen supply. *Front. Microbiol.*, 7, 557 (2016).
- 39. A. Pandey, C. Larroche, S. C. Ricke, (Eds.), *Biofuels: alternative feedstocks and conversion processes*. Academic Press (2011).

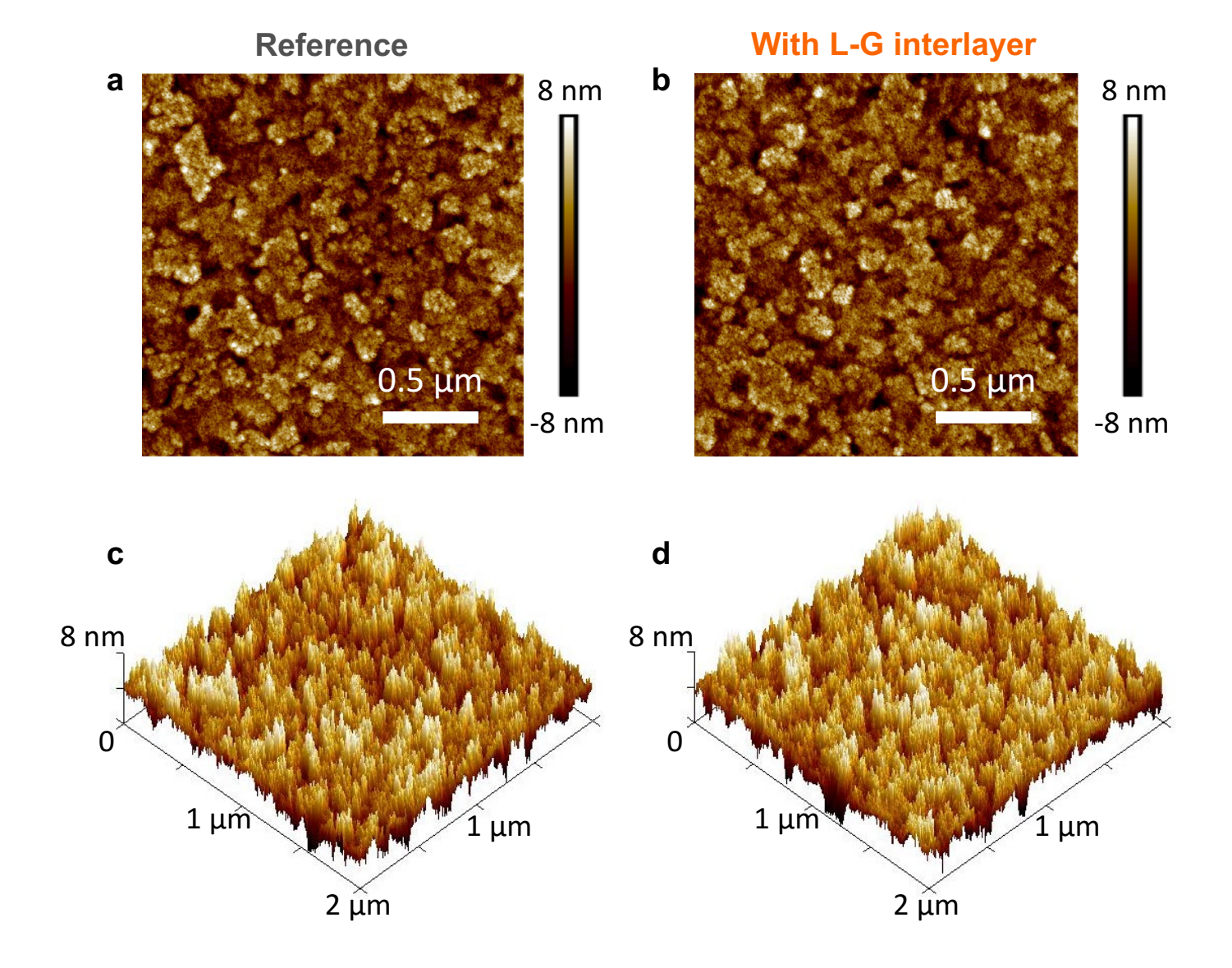


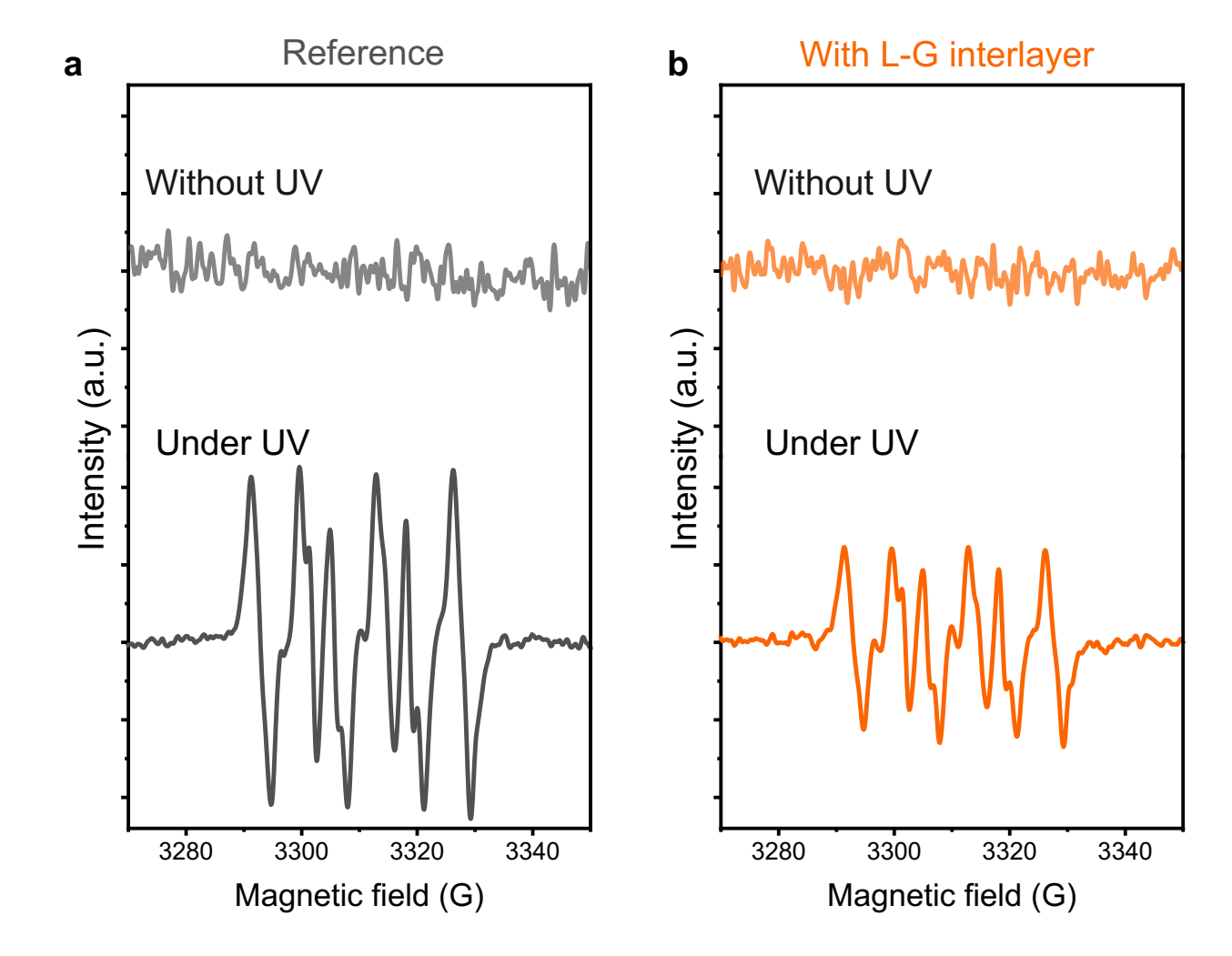




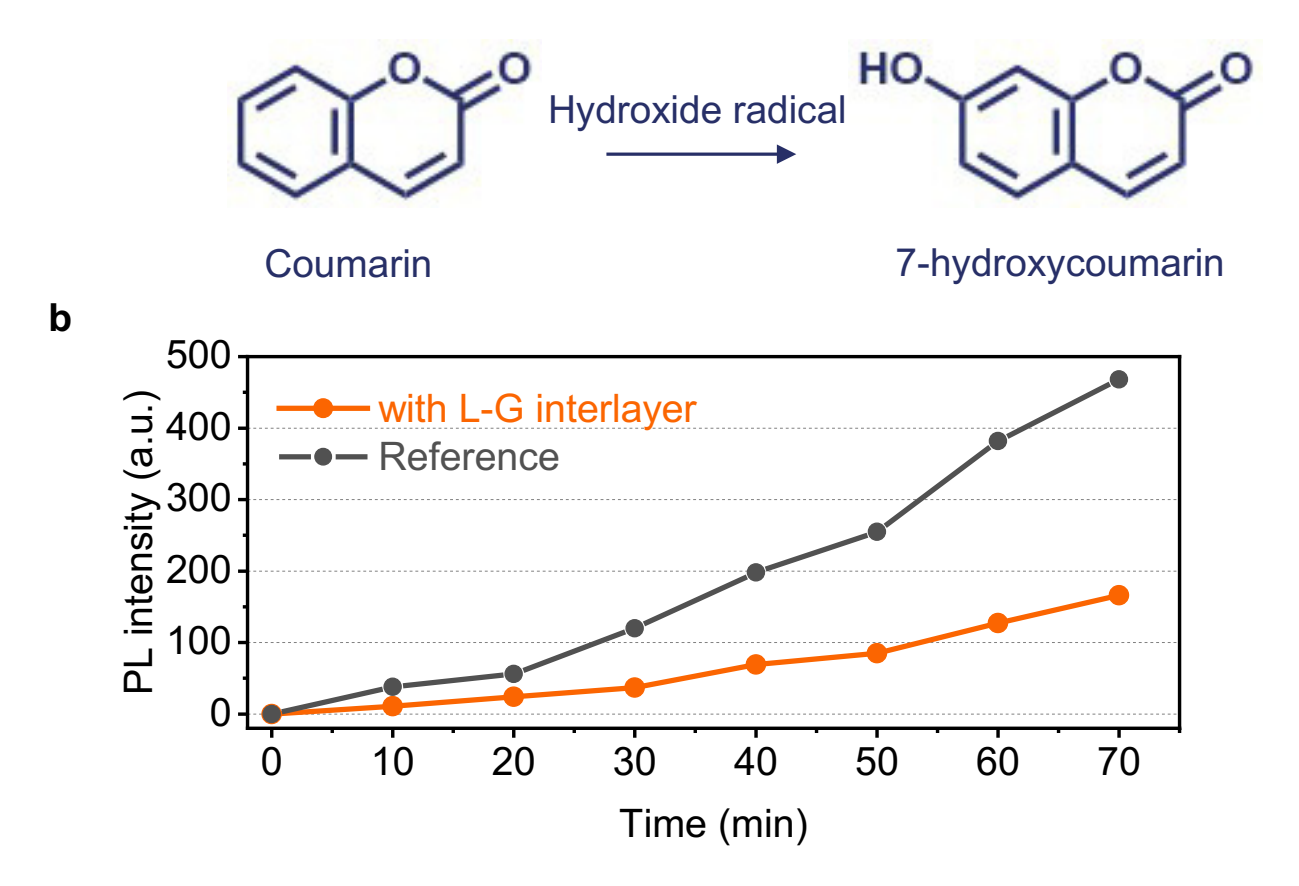


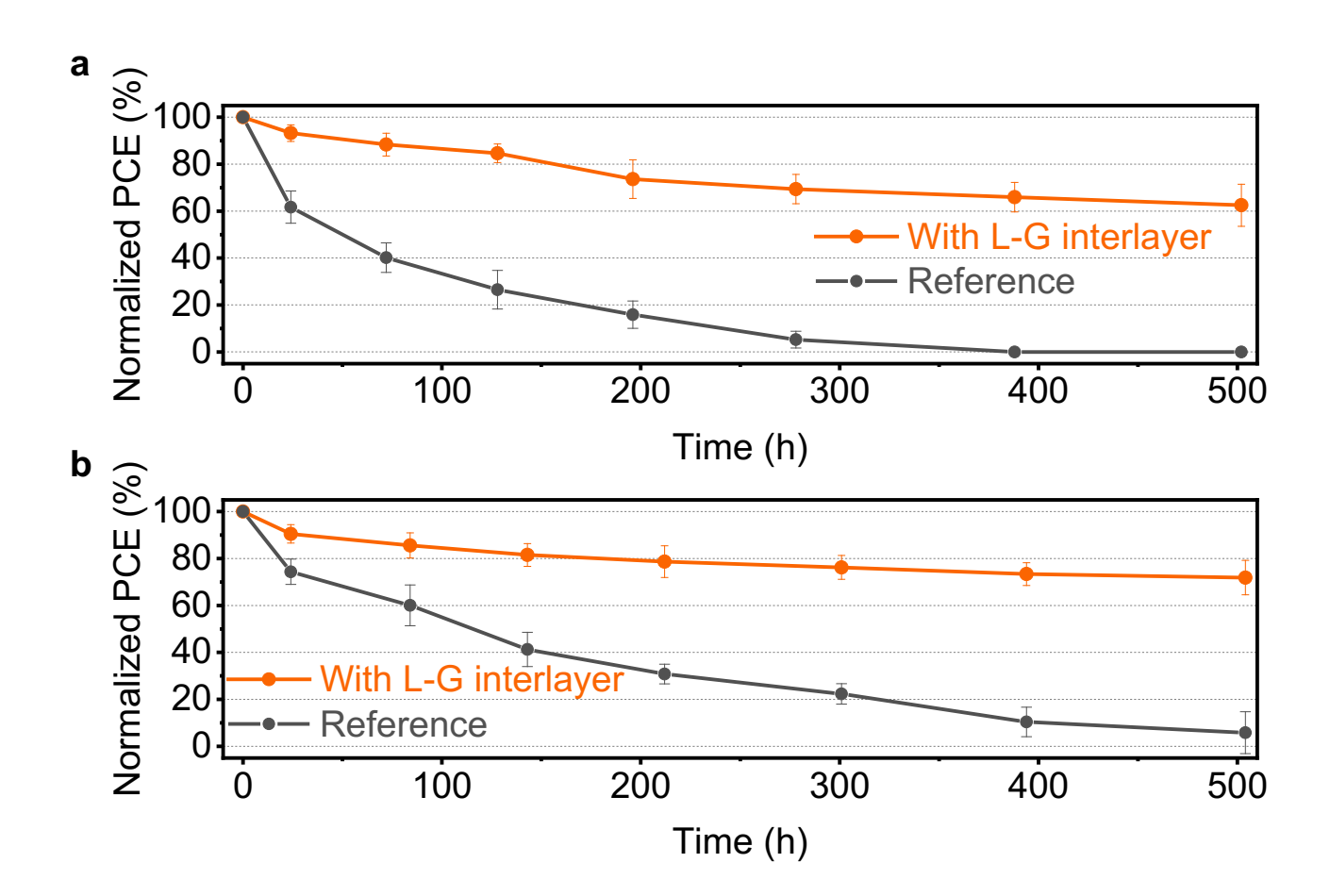


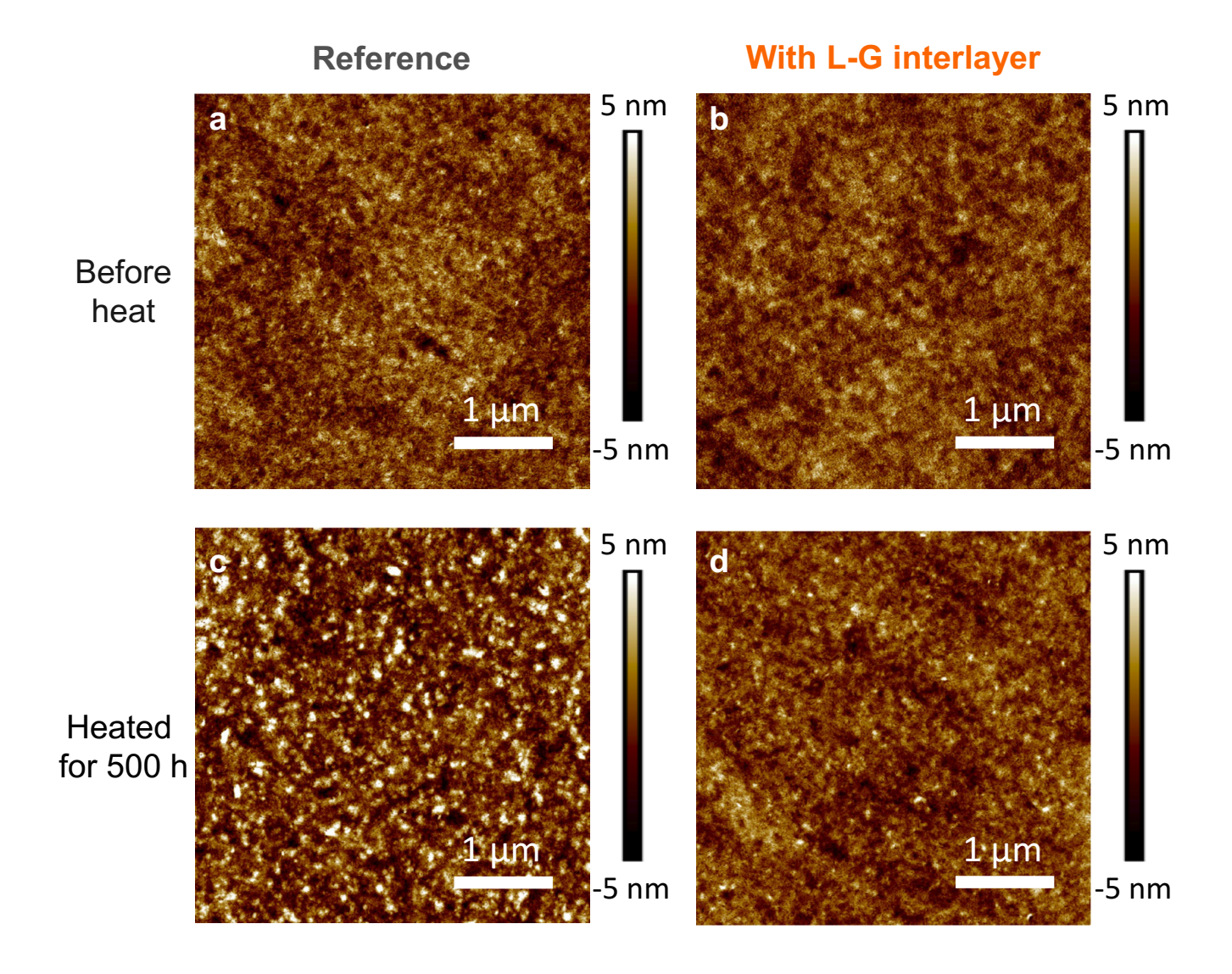




a







# Mung Bean Spatially-segmented inorganic solar cell Semitransparent Transparent OPV glass Day 0 Day 2 Day 4 Day 6 Day 8

Spatially-segmented Semitransparent Transparent Wheat inorganic solar cell **OPV** glass Day 0 Day 2 Day 4 Day 6 Day 8

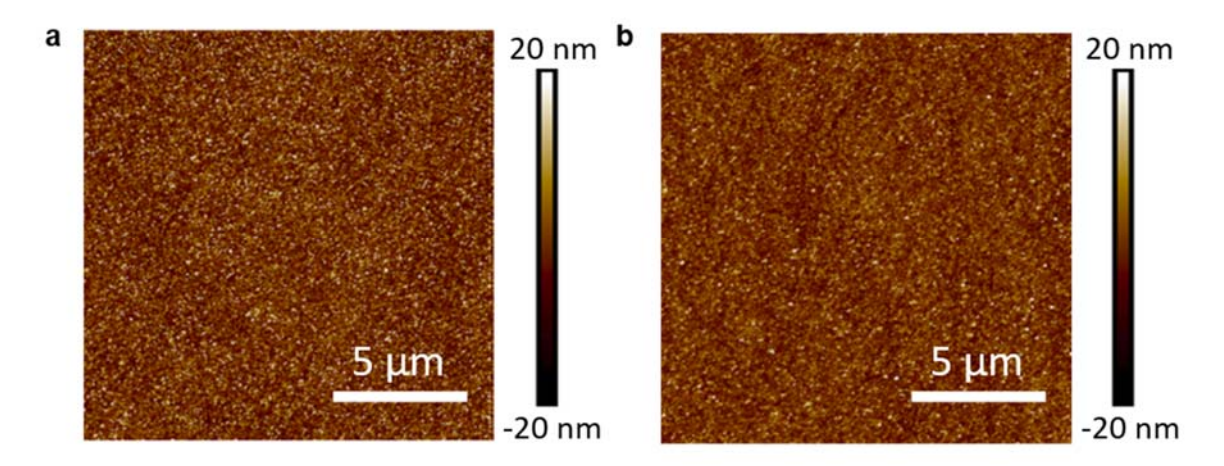
Spatially-segmented Semitransparent Transparent Broccoli inorganic solar cell **OPV** glass Day 0 Day 2 Day 4 Day 6 Day 8

### **Table of Contents**

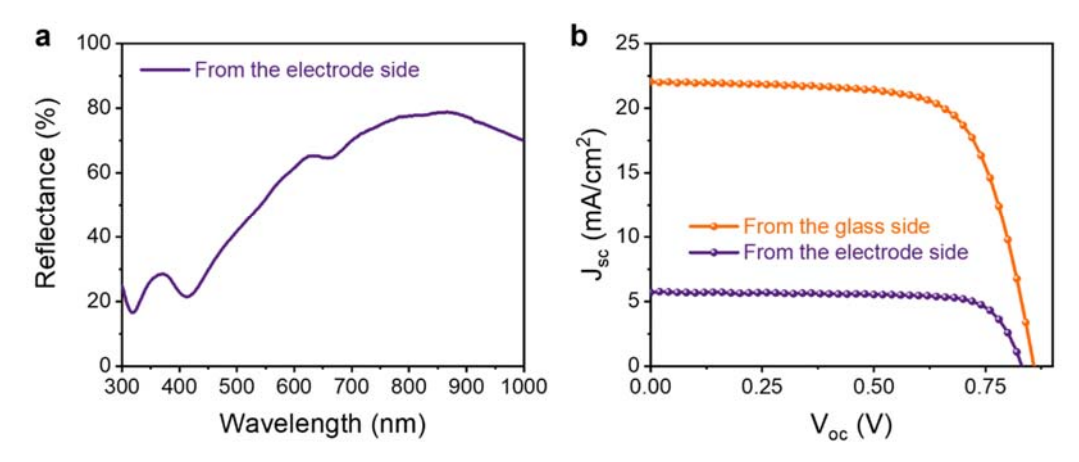
Supplementary Figures	2
Supplementary Fig. 1	
Supplementary Fig. 2.	
Supplementary Fig. 3.	4
Supplementary Fig. 4.	5
Supplementary Fig. 5.	6
Supplementary Fig. 6.	7
Supplementary Fig. 7.	8
Supplementary Fig. 8.	9
Supplementary Fig. 9.	10
Supplementary Tables	11
Supplementary Table 1.	11
Supplementary Table 2.	12
Supplementary Table 3.	13
Supplementary Table 4.	21
Supplementary Table 5.	29

### **Supplementary Figures**

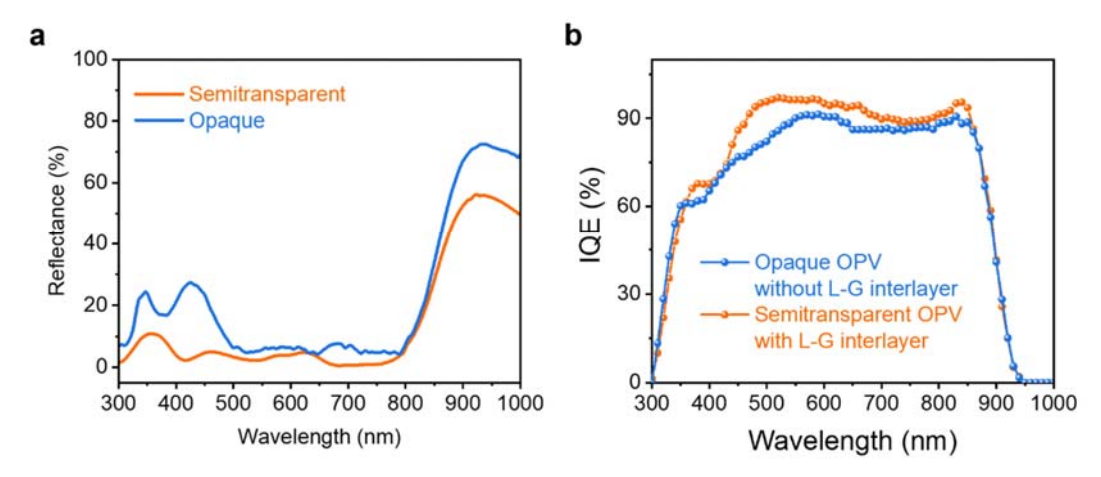
Supplementary Fig. 1. Molecular structures of donor (PM6), acceptor (Y6).



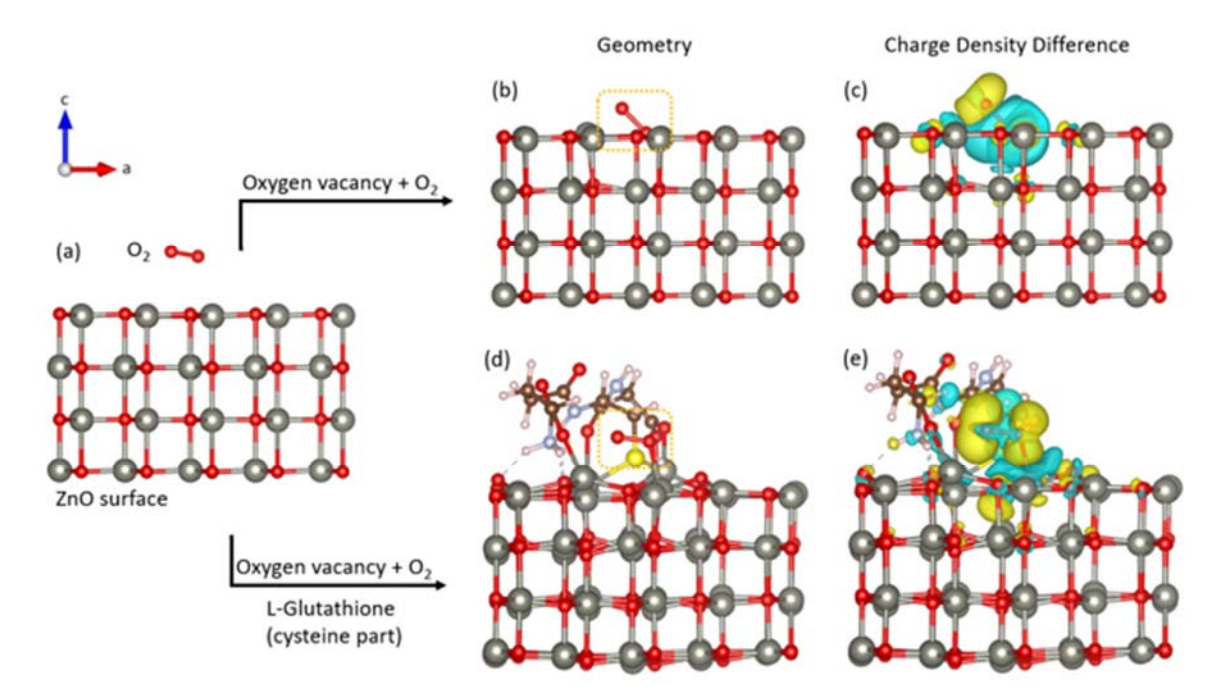
**Supplementary Fig. 2.** AFM images of the ZnO surface **(a)** with and **(b)** without the L-G interlayer (large scale).



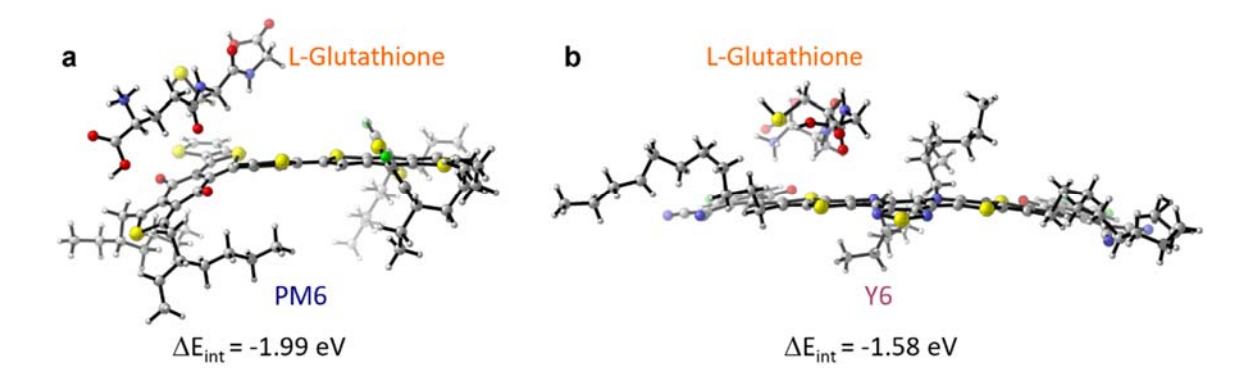
**Supplementary Fig.3.** (a) Reflectance measurement of the device with the L-G interlayer from the Ag side. (b) J-V curves of the devices with the L-G interlayer with sunlight from the glass side and the Ag side.



**Supplementary Fig. 4.** (a) Reflectance spectra and (b) the internal quantum efficiency (IQE) spectra of the semitransparent device with the L-G interlayer and the opaque device without the L-G interlayer.



**Supplementary Fig. 5. (a)** Perfect ZnO surface and oxygen molecule. **(b)** The optimized geometry of oxygen molecule and ZnO surface with oxygen vacancy and **(c)** its charge density difference. **(d)** The optimized geometry of oxygen molecule and L-G treated ZnO surface with oxygen vacancy and **(e)** its charge density difference.



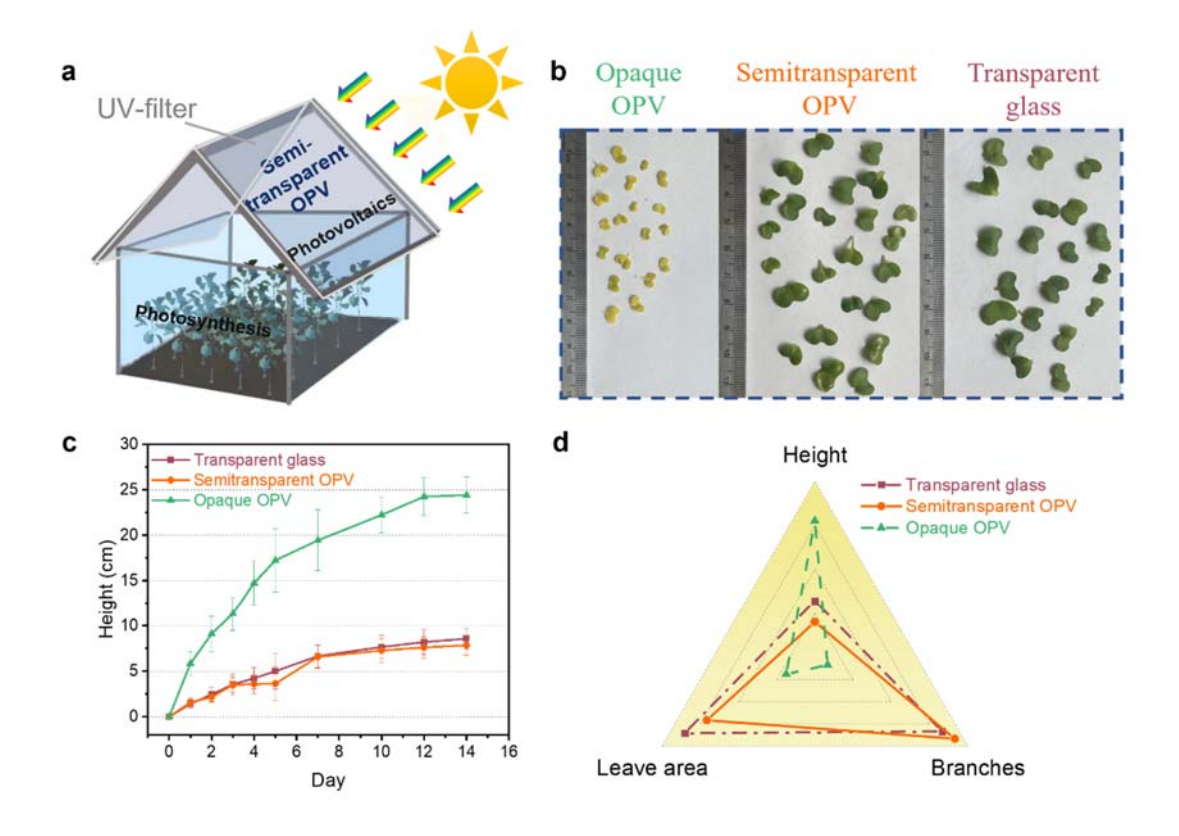
**Supplementary Fig. 6.** Simulation of the interaction energy between (a) L-G molecule and PM6 monomer and (b) L-G molecule and Y6 molecule.



**Supplementary Fig. 7.** Assembled greenhouse with semitransparent organic solar cell roof (the walls were covered with black tape and aluminum foil in the actual experiments).



Supplementary Fig. 8. Photos of the greenhouses with roofs of spatially segmented inorganic solar cell, semitransparent OPV, and transparent glass and the walls covered with reflective material.



Supplementary Fig. 9. (a) Scheme of the power-generating greenhouse with semitransparent OPV roof with UV-filter on it. (b) The images and sizes of the hearty broccolis sprouts after two-week growth in greenhouses with transparent glass, semitransparent OPV, and opaque OPV roofs with UV filters. (c) The height changes of the hearty broccolis sprouts growing in greenhouses with transparent glass, semitransparent OPV, and opaque OPV roofs in the two weeks. For each condition, 100 plants were harvested and measured for statistical analysis. Centre is the median value. Error bars indicate the standard deviation from these samples. (d) Plant growth evaluation of the hearty broccolis sprouts including height, branches, and leave area after two-week growth under different roofing materials.

## **Supplementary Tables**

**Supplementary Table 1.** Photoelectric performances of the devices with the L-G interlayer with sunlight from the glass side and the Ag side.

Condition (PM6/Y6 with L-G interlayer)	Voc (V)	Jsc (mA/cm <sup>2</sup> )	FF (%)	PCE (%)
From the glass side	0.86	22.2	70.4	13.5
From the Ag side	0.83	5.7	76.5	3.6

**Supplementary Table 2.** Biomass productivity of hearty wheat, broccoli sprout, and mung bean sprout growing in the greenhouses with roofs of transparent glass, the semitransparent organic solar cell panel, and segmented organic solar cell panel in 8 days.

	Greenhouse	Biomass	Electricity production
	Panel	productivity (g/day)	(Wh/day)
	Transparent glass	0.30	N/A
Mung bean	Semitransparent OPV	0.56	40.8
	Segmented PV	0.56	59.3
	Transparent glass	0.57	N/A
Wheat	Semitransparent OPV	0.58	43.6
	Segmented PV	0.55	63.4
	Transparent glass	0.74	N/A
Broccoli	Semitransparent OPV	0.82	33.1
	Segmented PV	0.81	48.1

Supplementary Table 3. Environmental conditions during the plant growth of mung bean.

Day – Time (GMT-7)	GHI (W/m <sup>2</sup> )	Temperature (°C)	Humidity (%)
Day 1-0	0	18.9	84
Day 1-1	0	18.3	87
Day 1-2	0	18.3	87
Day 1-3	0	17.8	90
Day 1-4	0	17.8	87
Day 1-5	1	18.9	87
Day 1-6	38	18.9	87
Day 1-7	175	20	75
Day 1-8	463	21.1	66
Day 1-9	674	23.3	59
Day 1-10	833	23.3	66
Day 1-11	946	23.9	62
Day 1-12	1001	23.9	64
Day 1-13	983	22.8	66
Day 1-14	927	22.8	66
Day 1-15	814	22.8	66
Day 1-16	653	22.2	71
Day 1-17	459	21.7	73
Day 1-18	255	20.6	75
Day 1-19	72	19.4	79
Day 1-20	0	18.9	84
Day 1-21	0	18.3	84
Day 1-22	0	18.3	84

Day 1-23	0	18.3	84
Day 2-0	0	18.3	81
Day 2-1	0	18.3	84
Day 2-2	0	18.3	87
Day 2-3	0	18.3	87
Day 2-4	1	18.3	87
Day 2-5	85	17.8	84
Day 2-6	267	18.3	87
Day 2-7	431	18.9	84
Day 2-8	664	19.4	79
Day 2-9	847	21.7	70
Day 2-10	963	22.2	68
Day 2-11	1022	22.8	66
Day 2-12	1020	23.3	64
Day 2-13	958	23.3	64
Day 2-14	839	22.2	68
Day 2-15	670	22.8	66
Day 2-16	469	21.7	68
Day 2-17	260	21.1	73
Day 2-18	74	20	76
Day 2-19	0	19.4	76
Day 2-20	0	18.9	78
Day 2-21	0	18.3	84
Day 2-22	0	18.3	81
Day 2-23	0	18.3	84

Day 3-0	0	18.3	81
Day 3-1	0	17.8	84
Day 3-2	0	17.8	84
Day 3-3	0	17.2	87
Day 3-4	1	17.8	84
Day 3-5	87	17.2	87
Day 3-6	279	18.3	84
Day 3-7	492	19.4	79
Day 3-8	691	20.6	73
Day 3-9	856	21.1	68
Day 3-10	974	22.2	61
Day 3-11	1034	21.1	65
Day 3-12	1032	21.7	63
Day 3-13	968	22.8	61
Day 3-14	846	22.8	61
Day 3-15	678	21.7	66
Day 3-16	478	21.1	68
Day 3-17	266	20	73
Day 3-18	76	19.4	68
Day 3-19	0	18.9	75
Day 3-20	0	18.3	78
Day 3-21	0	18.3	70
Day 3-22	0	18.3	73
Day 3-23	0	17.8	75
Day 4-0	0	18.3	78

Day 4-1	0	17.8	80
Day 4-2	0	17.8	81
Day 4-3	0	17.2	84
Day 4-4	1	17.8	81
Day 4-5	33	17.2	84
Day 4-6	79	18.3	75
Day 4-7	223	19.4	68
Day 4-8	496	20.6	65
Day 4-9	839	21.1	55
Day 4-10	970	22.2	59
Day 4-11	1028	21.1	57
Day 4-12	1023	21.7	61
Day 4-13	957	22.8	61
Day 4-14	836	22.8	63
Day 4-15	669	21.7	63
Day 4-16	471	21.1	65
Day 4-17	261	20	68
Day 4-18	74	19.4	63
Day 4-19	0	18.9	70
Day 4-20	0	18.3	72
Day 4-21	0	18.3	70
Day 4-22	0	18.3	72
Day 4-23	0	17.8	75
Day 5-0	0	17.2	78
Day 5-1	0	17.2	78

Day 5-2	0	17.2	81
Day 5-3	0	16.7	80
Day 5-4	1	17.2	78
Day 5-5	66	16.7	80
Day 5-6	150	17.8	78
Day 5-7	212	18.9	73
Day 5-8	399	20	65
Day 5-9	807	20.6	63
Day 5-10	942	21.7	63
Day 5-11	999	22.8	57
Day 5-12	996	22.8	57
Day 5-13	933	22.2	59
Day 5-14	814	22.8	57
Day 5-15	649	22.2	61
Day 5-16	454	21.1	68
Day 5-17	249	20.6	68
Day 5-18	69	19.4	73
Day 5-19	0	18.3	78
Day 5-20	0	18.3	78
Day 5-21	0	18.3	81
Day 5-22	0	18.3	81
Day 5-23	0	17.2	84
Day 6-0	0	17.2	80
Day 6-1	0	17.2	84
Day 6-2	0	17.2	84

Day 6-3	0	16.7	84
Day 6-4	1	17.2	84
Day 6-5	70	16.7	80
Day 6-6	220	17.8	81
Day 6-7	361	18.9	78
Day 6-8	623	20	73
Day 6-9	818	20.6	68
Day 6-10	943	21.7	66
Day 6-11	1001	22.8	61
Day 6-12	998	22.8	61
Day 6-13	936	22.2	59
Day 6-14	820	22.8	62
Day 6-15	659	22.2	66
Day 6-16	465	21.1	68
Day 6-17	258	20.6	73
Day 6-18	73	19.4	75
Day 6-19	0	18.3	81
Day 6-20	0	18.3	84
Day 6-21	0	18.3	87
Day 6-22	0	18.3	81
Day 6-23	0	17.2	84
Day 7-0	0	18.3	84
Day 7-1	0	18.3	84
Day 7-2	0	17.8	87
Day 7-3	0	17.8	90

5 5 4	•	150	0.7
Day 7-4	0	17.8	87
Day 7-5	26	18.3	84
Day 7-6	73	18.9	81
Day 1-7	147	19.4	79
Day 7-8	326	20	76
Day 7-9	667	20.6	73
Day 7-10	951	22.2	73
Day 7-11	1016	22.2	66
Day 7-12	1019	22.2	66
Day 7-13	960	22.2	66
Day 7-14	843	22.2	66
Day 7-15	678	21.7	68
Day 7-16	479	21.1	71
Day 7-17	268	21.1	71
Day 7-18	77	20	73
Day 7-19	0	19.4	76
Day 7-20	0	18.9	78
Day 7-21	0	18.9	78
Day 7-22	0	18.9	81
Day 7-23	0	18.9	84
Day 8-0	0	18.3	84
Day 8-1	0	18.3	87
Day 8-2	0	18.3	84
Day 8-3	0	18.3	81
Day 8-4	1	17.8	84

Day 8-5	85	18.3	84
Day 8-6	280	18.9	81
Day 8-7	494	20.6	73
Day 8-8	694	21.7	68
Day 8-9	859	22.2	68
Day 8-10	976	22.8	66
Day 8-11	1036	22.8	66
Day 8-12	1034	23.9	62
Day 8-13	971	23.3	66
Day 8-14	850	22.8	66
Day 8-15	683	22.8	66
Day 8-16	482	22.2	68
Day 8-17	269	21.7	73
Day 8-18	76	20.6	75
Day 8-19	0	19.4	73
Day 8-20	0	19.4	76
Day 8-21	0	18.9	81
Day 8-22	0	18.9	81
Day 8-23	0	18.3	84

Supplementary Table 4. Environmental conditions during the plant growth of wheat.

Day – Time (GMT-7)	GHI (W/m <sup>2</sup> )	Temperature (°C)	Humidity (%)
Day 1-0	0	16.7	86
Day 1-1	0	16.7	86
Day 1-2	0	17.2	84
Day 1-3	0	17.2	84
Day 1-4	0	17.2	84
Day 1-5	0	17.2	81
Day 1-6	21	17.2	81
Day 1-7	58	17.8	78
Day 1-8	143	18.3	78
Day 1-9	301	18.9	75
Day 1-10	693	20	70
Day 1-11	950	20.6	68
Day 1-12	1013	21.1	65
Day 1-13	1014	21.1	63
Day 1-14	953	21.1	63
Day 1-15	836	20.6	65
Day 1-16	671	20.6	68
Day 1-17	473	20	70
Day 1-18	238	18.9	78
Day 1-19	70	18.3	81
Day 1-20	0	17.8	84
Day 1-21	0	17.8	80
Day 1-22	0	17.8	80
Day 1-23	0	17.2	81

Day 2-0	0	17.2	81
Day 2-1	0	17.2	81
Day 2-2	0	16.7	84
Day 2-3	0	16.7	84
Day 2-4	0	16.7	84
Day 2-5	0	16.7	84
Day 2-6	30	16.7	84
Day 2-7	76	17.2	81
Day 2-8	194	17.8	78
Day 2-9	483	18.3	78
Day 2-10	828	19.4	73
Day 2-11	944	20	68
Day 2-12	1002	20.6	65
Day 2-13	998	21.1	65
Day 2-14	934	21.1	68
Day 2-15	814	20.6	68
Day 2-16	650	20	70
Day 2-17	456	19.4	73
Day 2-18	249	18.3	78
Day 2-19	67	17.8	80
Day 2-20	0	17.2	84
Day 2-21	0	17.2	87
Day 2-22	0	17.2	84
Day 2-23	0	17.8	84
Day 3-0	0	17.8	80

Day 3-1	0	17.8	80
Day 3-2	0	17.8	84
Day 3-3	0	17.8	84
Day 3-4	0	17.8	84
Day 3-5	0	17.8	84
Day 3-6	64	17.8	84
Day 3-7	241	18.3	81
Day 3-8	446	19.4	76
Day 3-9	639	20	73
Day 3-10	798	20.6	70
Day 3-11	911	21.1	68
Day 3-12	971	21.1	68
Day 3-13	970	21.7	66
Day 3-14	910	21.7	66
Day 3-15	792	21.7	68
Day 3-16	628	21.1	68
Day 3-17	432	20.6	70
Day 3-18	228	20	73
Day 3-19	56	19.4	76
Day 3-20	0	18.9	78
Day 3-21	0	18.3	84
Day 3-22	0	18.3	84
Day 3-23	0	18.3	87
Day 4-0	0	18.3	87
Day 4-1	0	17.8	87

Day 4-2	0	17.8	87
Day 4-3	0	17.8	87
Day 4-4	0	17.8	90
Day 4-5	0	17.8	87
Day 4-6	52	17.8	90
Day 4-7	196	17.8	90
Day 4-8	426	18.3	87
Day 4-9	626	19.4	81
Day 4-10	787	21.1	73
Day 4-11	902	21.1	73
Day 4-12	965	21.1	73
Day 4-13	966	21.7	70
Day 4-14	908	21.7	70
Day 4-15	794	20.6	75
Day 4-16	633	20	78
Day 4-17	441	20	78
Day 4-18	236	18.9	81
Day 4-19	60	18.9	81
Day 4-20	0	18.9	78
Day 4-21	0	18.9	84
Day 4-22	0	18.9	84
Day 4-23	0	18.9	81
Day 5-0	0	18.9	84
Day 5-1	0	17.8	90
Day 5-2	0	17.8	90

Day 5-3	0	17.2	93
Day 5-4	0	17.2	93
Day 5-5	0	17.2	93
Day 5-6	58	17.2	93
Day 5-7	229	17.2	93
Day 5-8	435	17.8	90
Day 5-9	631	19.4	81
Day 5-10	794	20.6	75
Day 5-11	910	21.7	73
Day 5-12	969	21.7	73
Day 5-13	969	22.2	71
Day 5-14	908	22.2	71
Day 5-15	792	21.7	73
Day 5-16	632	21.1	71
Day 5-17	439	21.1	73
Day 5-18	233	20.6	78
Day 5-19	57	19.4	84
Day 5-20	0	18.9	87
Day 5-21	0	19.4	84
Day 5-22	0	19.4	81
Day 5-23	0	18.3	87
Day 6-0	0	18.9	84
Day 6-1	0	18.3	87
Day 6-2	0	17.8	90
Day 6-3	0	17.8	90

Day 6-4	0	17.8	90
Day 6-5	0	17.8	90
Day 6-6	46	17.8	93
Day 6-7	230	18.9	87
Day 6-8	433	20	81
Day 6-9	605	21.1	76
Day 6-10	775	25.6	60
Day 6-11	896	26.7	56
Day 6-12	927	24.4	64
Day 6-13	750	23.3	68
Day 6-14	902	23.3	68
Day 6-15	788	22.2	73
Day 6-16	627	22.8	71
Day 6-17	433	22.2	73
Day 6-18	228	21.7	76
Day 6-19	55	20.6	78
Day 6-20	0	20	81
Day 6-21	0	20.6	78
Day 6-22	0	21.1	76
Day 6-23	0	22.8	68
Day 7-0	0	21.1	76
Day 7-1	0	20.6	78
Day 7-2	0	20	84
Day 7-3	0	20	81
Day 7-4	0	20	81

Day 7-5	0	20	81
Day 7-6	48	20.6	84
Day 1-7	221	21.7	78
Day 7-8	433	24.4	67
Day 7-9	629	25	66
Day 7-10	793	25.6	64
Day 7-11	909	24.4	69
Day 7-12	969	24.4	69
Day 7-13	969	23.9	69
Day 7-14	908	22.8	71
Day 7-15	792	22.8	68
Day 7-16	630	22.2	71
Day 7-17	436	21.7	73
Day 7-18	232	21.1	76
Day 7-19	57	20	78
Day 7-20	0	19.4	84
Day 7-21	0	19.4	84
Day 7-22	0	19.4	84
Day 7-23	0	19.4	84
Day 8-0	0	18.9	87
Day 8-1	0	18.9	87
Day 8-2	0	18.3	90
Day 8-3	0	17.8	93
Day 8-4	0	17.8	90
Day 8-5	0	17.8	90

Day 8-6	63	18.3	90
Day 8-7	245	18.3	90
Day 8-8	454	18.9	87
Day 8-9	652	20	78
Day 8-10	816	21.1	73
Day 8-11	933	22.8	68
Day 8-12	994	23.3	64
Day 8-13	993	23.9	62
Day 8-14	932	23.9	62
Day 8-15	814	23.3	64
Day 8-16	650	23.3	66
Day 8-17	452	22.2	68
Day 8-18	241	21.7	73
Day 8-19	59	21.1	76
Day 8-20	0	20	81
Day 8-21	0	19.4	84
Day 8-22	0	19.4	84
Day 8-23	0	19.4	87

Supplementary Table 5. Environmental conditions during the plant growth of broccoli.

Day – Time (GMT-7)	GHI (W/m <sup>2</sup> )	Temperature (°C)	Humidity (%)
Day 1-0	0	18.9	81
Day 1-1	0	18.9	81
Day 1-2	0	19.4	81
Day 1-3	0	19.4	81
Day 1-4	0	20	78
Day 1-5	0	19.4	84
Day 1-6	21	19.4	84
Day 1-7	74	20	81
Day 1-8	175	20.6	78
Day 1-9	399	21.1	76
Day 1-10	790	22.2	71
Day 1-11	920	23.3	68
Day 1-12	986	23.9	64
Day 1-13	989	23.3	66
Day 1-14	930	22.8	68
Day 1-15	813	22.2	71
Day 1-16	648	21.1	73
Day 1-17	449	20	78
Day 1-18	231	19.4	79
Day 1-19	54	18.9	81
Day 1-20	0	18.3	84
Day 1-21	0	18.3	84
Day 1-22	0	18.3	84
Day 1-23	0	17.8	87

Day 2-0	0	18.3	84
Day 2-1	0	17.8	87
Day 2-2	0	17.8	90
Day 2-3	0	17.8	90
Day 2-4	0	17.8	90
Day 2-5	0	18.3	84
Day 2-6	28	18.9	81
Day 2-7	90	19.4	79
Day 2-8	186	19.4	79
Day 2-9	356	20	76
Day 2-10	665	21.7	70
Day 2-11	916	22.2	66
Day 2-12	980	22.8	64
Day 2-13	982	22.8	64
Day 2-14	923	22.2	68
Day 2-15	807	22.2	68
Day 2-16	642	21.1	73
Day 2-17	444	20.6	73
Day 2-18	233	19.4	79
Day 2-19	52	18.9	81
Day 2-20	0	18.3	81
Day 2-21	0	18.3	81
Day 2-22	0	17.8	84
Day 2-23	0	17.8	84
Day 3-0	0	17.8	84

Day 3-1	0	17.8	87
Day 3-2	0	17.8	87
Day 3-3	0	17.8	84
Day 3-4	0	17.8	84
Day 3-5	0	18.3	81
Day 3-6	22	18.3	81
Day 3-7	67	18.3	81
Day 3-8	238	18.9	81
Day 3-9	543	20	76
Day 3-10	788	22.2	66
Day 3-11	906	22.8	64
Day 3-12	968	22.2	66
Day 3-13	924	22.8	66
Day 3-14	906	22.8	66
Day 3-15	787	22.2	68
Day 3-16	621	21.7	70
Day 3-17	423	20	78
Day 3-18	216	18.9	81
Day 3-19	46	18.3	84
Day 3-20	0	18.9	81
Day 3-21	0	18.3	84
Day 3-22	0	18.9	84
Day 3-23	0	18.9	81
Day 4-0	0	18.3	84
Day 4-1	0	18.3	81

Day 4-2	0	18.3	84
Day 4-3	0	18.3	84
Day 4-4	0	18.3	84
Day 4-5	0	18.3	84
Day 4-6	18	18.9	81
Day 4-7	63	19.4	79
Day 4-8	150	20	78
Day 4-9	318	20.6	75
Day 4-10	587	22.2	68
Day 4-11	817	23.9	62
Day 4-12	884	22.8	66
Day 4-13	879	23.9	62
Day 4-14	772	22.8	66
Day 4-15	448	22.2	68
Day 4-16	425	22.2	68
Day 4-17	370	21.7	70
Day 4-18	176	20.6	76
Day 4-19	33	20	78
Day 4-20	0	19.4	84
Day 4-21	0	19.4	84
Day 4-22	0	19.4	81
Day 4-23	0	19.4	79
Day 5-0	0	2.8	81
Day 5-1	0	19.4	81
Day 5-2	0	18.9	81

Day 5-3	0	19.4	79
Day 5-4	0	18.9	81
Day 5-5	0	18.9	81
Day 5-6	28	19.4	81
Day 5-7	173	20.6	75
Day 5-8	368	21.7	70
Day 5-9	562	23.9	62
Day 5-10	726	23.3	66
Day 5-11	844	23.3	66
Day 5-12	906	24.4	62
Day 5-13	906	24.4	62
Day 5-14	843	24.4	62
Day 5-15	724	23.9	66
Day 5-16	558	23.3	68
Day 5-17	362	22.8	71
Day 5-18	168	21.7	78
Day 5-19	32	21.1	78
Day 5-20	0	20.6	81
Day 5-21	0	20.6	81
Day 5-22	0	20.6	81
Day 5-23	0	20.6	81
Day 6-0	0	20.6	78
Day 6-1	0	20	78
Day 6-2	0	20	78
Day 6-3	0	20	78

Day 6-4	0	20	78
Day 6-5	0	20	78
Day 6-6	12	20	81
Day 6-7	37	20.6	78
Day 6-8	84	21.1	76
Day 6-9	180	22.2	71
Day 6-10	149	23.3	66
Day 6-11	215	24.4	67
Day 6-12	629	24.4	67
Day 6-13	543	23.3	71
Day 6-14	469	22.8	73
Day 6-15	533	22.8	73
Day 6-16	514	23.9	69
Day 6-17	384	23.3	71
Day 6-18	181	22.8	73
Day 6-19	34	21.7	81
Day 6-20	0	20.6	87
Day 6-21	0	20.6	87
Day 6-22	0	20.6	84
Day 6-23	0	20.6	84
Day 7-0	0	20.6	84
Day 7-1	0	21.1	81
Day 7-2	0	21.7	78
Day 7-3	0	21.7	78
Day 7-4	0	21.7	78

Day 7-5	0	21.1	81
Day 7-6	32	21.7	78
Day 1-7	197	23.3	71
Day 7-8	402	25	58
Day 7-9	594	25	64
Day 7-10	709	25.6	64
Day 7-11	497	26.1	60
Day 7-12	688	25.6	62
Day 7-13	793	26.1	60
Day 7-14	770	26.1	62
Day 7-15	687	25.6	64
Day 7-16	425	24.4	69
Day 7-17	363	23.9	69
Day 7-18	201	22.2	76
Day 7-19	32	21.7	78
Day 7-20	0	21.7	78
Day 7-21	0	21.7	81
Day 7-22	0	21.1	84
Day 7-23	0	21.1	84
Day 8-0	0	21.1	84
Day 8-1	0	21.1	84
Day 8-2	0	20.6	87
Day 8-3	0	20.6	87
Day 8-4	0	20.6	87
Day 8-5	0	20.6	87

Day 8-6	35	21.1	84
Day 8-7	172	21.7	78
Day 8-8	396	22.2	76
Day 8-9	608	22.2	76
Day 8-10	765	22.8	73
Day 8-11	887	23.9	69
Day 8-12	946	24.4	67
Day 8-13	889	24.4	67
Day 8-14	843	25.6	58
Day 8-15	637	24.4	64
Day 8-16	535	23.3	66
Day 8-17	511	22.8	73
Day 8-18	358	21.7	78
Day 8-19	147	21.1	81
Day 8-20	0	20.6	84
Day 8-21	0	20.6	84
Day 8-22	0	20	84
Day 8-23	0	20	84